INTEGRATING HIGH THROUGHPUT DATA WITH SPATIAL SYSTEM PHARMACOLOGY MODEL TO PREDICT IMMUNOTHERAPY RESPONSE FOR TRIPLE NEGATIVE BREAST CANCER

by

Shuming Zhang

A thesis submitted to Johns Hopkins University in conformity with the requirements for the degree of Master of Science in Biomedical Engineering

Baltimore, Maryland

April 2021

Abstract:

Response to cancer immunotherapies depends on the complex and dynamic interactions between T cell recognition and killing of tumor cells that are counteracted through immunosuppressive pathways in the tumor microenvironment. Therefore, while measurements such as tumor mutational burden provide biomarkers to select patients for immunotherapy, they neither universally predict patient post-treatment outcome nor imply the mechanisms that underlie immunotherapy resistance. Recent advances in single cell RNA sequencing technology (scRNA-seq) measure cellular heterogeneity within cells of an individual tumor but have yet to realize the promise of predictive oncology. In addition to data, mechanistic multiscale computational models are being developed for predicting cellular states during tumor progression and treatment response. Incorporating single cell data from a tumor to parameterize these computational models can lead to a deeper insight into subsequent tumor progression and predictions of clinical outcome in an individual. While the high dimensionality of single cell analysis data poses a challenge for integration, Quantitative System Pharmacology (QSP) models incorporate discrete cellular states that can be obtained directly from single cell data. Here, we integrate whole exome sequencing and scRNA-seq data from Triple Negative Breast Cancer (TNBC) patients to model neoantigen burden in tumor cells as input to a spatial Quantitative System Pharmacology (spQSP) model that comprises four compartments (tumor, tumor-draining lymph node, central and peripheral) to represent a whole patient and uses spatial agent-based model (ABM) to represent tumor volumes at the cellular scale. We use the high-throughput single-cell data to model the role of antigen burden and heterogeneity relative to the tumor microenvironment composition on predicted immunotherapy response. Using this model, we found that patients with more tumor neoantigens have better responses to immunotherapy. In

addition, patients with more heterogeneous neoantigen profile in cancer cells are predicted with worse treatment outcomes. This thesis demonstrates the feasibility of merging high throughput data to initialize cell states in multiscale computational models such as the spQSP for personalized prediction of tumor outcomes to immunotherapy.

Primary Reader(s) and Advisor(s): Dr. Aleksander S. Popel and Dr. Elana J. Fertig

Contents

List of Tables

List of Figures

1. Introduction:

Breast cancer is the most frequently diagnosed and leading cause of cancer death among female population in the world (Bray et al., 2018). Triple Negative Breast Cancer (TNBC), which is defined as the type of breast cancer characterized by absence of expression of estrogen receptor (ER), progesterone receptor (PR) and Erb-B2 receptor tyrosine-protein kinase (HER2), has the poorest treatment outcome among all breast cancer subtypes due to lack of therapeutic molecular targets. Whereas other hormone receptor positive subtypes of breast cancer benefit from targeted therapies, the absence of receptor expression does not allow for such precision therapeutic selection in this cancer type. Immunotherapies that reinvigorate the host's immune system to eradicate cancer cells have emerged as promising alternatives to chemotherapy and targeted therapy(Benvenuto et al., 2019). To that end, immune-checkpoint inhibitor (ICI) therapy or immunotherapy including nivolumab, pembrolizumab (anti-PD1), atezolizumab, durvalumab (anti-PDL1), ipilimumab, tremelimumab (anti-CTLA4) were studied in multiple clinical trials among TNBC patients to investigate efficacy of immunotherapy in either monotherapy or combination therapy (Bianchini et al., 2016). The Objective Response Rate (ORR) ranges from 4.8% to 62% for all recent TNBC clinical trials involving different types of ICIs (Emens, 2021; Malhotra & Emens, 2020; Planes-Laine et al., 2019). The wide range of ORR suggests the need for effective, mechanistic biomarkers to predict treatment outcome for individual patients. All abbreviations are presented in Table 1.

Term	Abbreviation
Agent-based model	ABM
Antigen Presenting Cell	APC
Arginase-1	Arg-I
Chemokine (C-C motif) ligand 2	CCL2
Cancer stem-like cell	CSC
Cytotoxic T lymphocytes	CTL
Cytotoxic T-lymphocyte-associated protein 4	CTLA-4
Immune Checkpoint Inhibitor	ICI
Interferon gamma	IFNγ
Interleukin 2	IL-2
Latin Hypercube Sampling	LHS
Myeloid Derived Suppressor Cell	MDSC
Nitric Oxide	NO
Ordinary Differential Equation	ODE
Programmed cell death protein 1	PD-1
Partial Differential Equation	PDE
Programmed death-ligand 1 (2)	PD-L1 (2)
Quantitative System Pharmacology	QSP
Region of Interest	ROI
Single cell RNA sequencing	scRNA-seq
Tumor Mutational Burden	TMB
Tumor Microenvironment	TME
Tumor Specific Neoantigen	TSA

Table 1: Table of abbreviations used in this thesis.

The interplay between the immune cells and malignant cells within the tumor ultimately drive successful response to ICI. Within the tumor cells, tumor mutational burden (TMB), defined as total number of somatic mutations per megabase in tumor genome, has been recognized as a biomarker to predict effectiveness of immunotherapy in multiple clinical trials (Brown et al., 2014; Fumet et al., 2020). The greater number of mutations reflected in higher TMB correlates with a higher probability of neoantigens, which can be recognized by T cells to elicit immune response (Jiang et al., 2019). However, other studies have shown high TMB cannot guarantee patients' responses to immunotherapy due to either insufficient immune cell infiltration or therapeutic resistance resulting from tumor cell heterogeneity (Kazdal et al., 2019; Maleki Vareki, 2018). Tumor heterogeneity has three major sources: genetic, phenotypic, and

microenvironmental. Intratumoral heterogeneity leads to acquired resistance during treatments, and intertumoral heterogeneity leads to different patients response to the same treatment (Marusyk et al., 2020). Experimental studies have further demonstrated that high expression of diverse neoantigens can lead to reduced immune attack over systems with similar expression of a homogeneous population of neoantigens(Gejman et al., 2018). Thus, predicting individual outcomes to ICI could be enhanced by extending from population-level biomarkers to modeling the impact of this tumor and immune cell heterogeneity within individual tumors.

Advanced omics technologies spanning DNA, RNA, and proteomic scales have enabled researchers to gain deeper insight of tumor heterogeneity at individual patient's level. Many groups characterize immune cell landscape through single cell RNA sequencing data (scRNA-seq) for various types of cancer (Azizi et al., 2018; Guo et al., 2018; L. Ma et al., 2019; Zhang et al., 2019; Zheng et al., 2017). These technologies can be used both to determine immune cell composition in the tumor microenvironment (TME) along with the molecular states of tumor cells(Lim et al., 2020). These technologies have been widely applied to study the state of breast tumors(Azizi et al., 2018). Likewise resolved molecular profiling technologies provide further opportunities to characterize the tumor microenvironment(Jackson et al., 2020; Keren et al., 2018), but are only just emerging at high-dimensional molecular resolution to characterize the pathways in both tumor and immune cells(Andersson et al., 2020; He et al., 2020). Characterizing the heterogeneous molecular and cellular states with greater resolution helps not only to identify novel biomarkers, but also to understand the significance of these pathways and inter-cellular interactions in ICI response.

At the same time as high-throughput tumor atlases are emerging, mechanistic computational models are also developing as powerful tools to predict patients' responses to

cancer immunotherapy(Rozenblatt-Rosen et al., 2020). For instance, Quantitative System Pharmacology (QSP) models that simulate biological processes, pharmacokinetics (PK), and pharmacodynamics (PD) of selected drugs, have becomes an indispensable tool for drug discovery and designing dosing regimen (Bai et al., 2019; Helmlinger et al., 2019; Sové et al., 2020). QSP models are often validated by results of clinical trials to reflect their predictive power (Jafarnejad et al., 2019; H. Ma et al., 2020; Wang et al., 2020, 2021). Despite QSP models' ability to reasonably reproduce clinical outcome at population level, due to their compartmental nature and their lumped representation of tumor the models are unable to characterize cellular or spatial heterogeneity for individual patients. To address that issue, Gong et al. developed a multiscale agent-based model (ABM) to simulate spatio-temporal tumor progression and simulation results can be visualized with single cell resolution (Gong et al., 2017). Further integrating omics data into QSP models can parameterize these models for individual patients, providing the prospect to simulate a virtual patients' longitudinal response to various therapeutic regimens. Lazarou et al. proposed integrating omics data into QSP models at multiscale levels (tissue, cellular, and molecular) (Lazarou et al., 2020). Johnson et al. integrated single cell RNA sequencing data with mechanistic model to improve predictive accuracy of chemotherapy responses (Johnson et al., 2020). The robust characterization of cellular heterogeneity by single cell technologies makes them ideally suited for integration with QSP models predicting ICI response.

In this study, we extend our spatial Quantitative System Pharmacology (spQSP) model to integrate single-cell RNA-sequencing data. We incorporate single cell sequencing data and whole exome sequencing data of triple negative breast cancer tumors from Chung et al. into a spQSP model(Chung et al., 2017) to enable patient-specific models. We leverage this model to

predict the impact of tumor neoantigen profiles and neoantigen heterogeneity on response to immunotherapy. Altogether, this integrated system provides a new framework to combine omics data of tumor cell heterogeneity with computational QSP model to model ICI response.

2. Methods

2.1 spQSP Platform Formulation

The spQSP model consists of two modules: a whole-patient QSP model and a tumor compartment-specific agent-based model (ABM). The QSP model is expressed in terms of ordinary differential equations (ODE) and algebraic equations that simulate tumor progression dynamics at organ level (Sové et al., 2020; Wang et al., 2020, 2021). The ABM, representing a $1mm \times 1mm \times 1mm$ region of interest in the tumor, that simulates spatio-temporal molecular and cellular interactions in three-dimensional space(Gong et al., 2017). Specifically, we modified the original framework to include the further effect of myeloid derived suppressor cells (MDSCs) and T cell recognition of antigens to better tailor this model to breast cancer. A schematic of the spQSP model comprising a whole-patient compartmental ordinary differential equation-based QSP model and a spatial agent-based model (ABM) representing a region-of-interest tumor volume is shown in Figure 1.

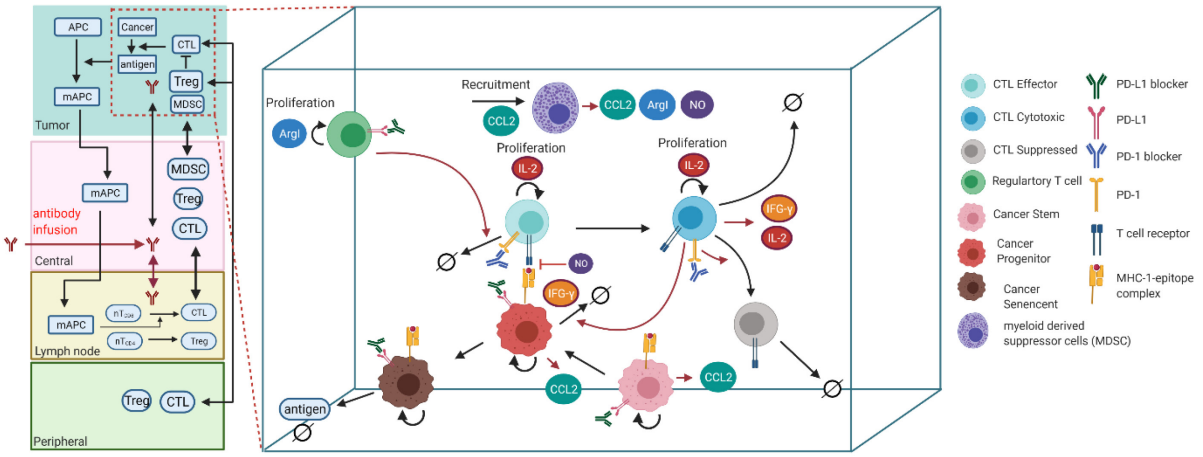

Figure 1: Schematic of the spQSP model, which is comprised of a QSP module and an ABM module. Left: The four-compartments QSP model is presented, including tumor, central blood, lymph node, and peripheral, which simulates the process of T cell priming, Immune cell trafficking, immune-cancer interactions, antigen collection and presentation. Right: ABM module partially represents the tumor compartment, which further model immune-tumor interactions spatial-temporally.

2.1.1 QSP module

The QSP model is comprised of four major compartments: Tumor compartment, where cancer cells proliferate and anti-tumoral activities take place; Lymph node, where naïve CD8+ T cell priming initiates with tumor neoantigen on antigen presenting cells (APCs) followed by T cell expansion; Central compartment represents blood in human body, transporting endogenous molecules, cells and drugs to different parts of the body; Peripheral compartment represents other organs in the body.

2.1.2 Agent rules in ABM

Current version of spQSP model is an extension of our previous immuno-oncology ABM model(Gong et al., 2017). Here we significantly extended the model by introducing additional cell types, detailed rules governing agents' interactions, and explicitly considered heterogeneous tumor neoantigens on cancer cells. In general, the ABM module has two distinct types of agents: cellular agents and molecular agents. There are four major cell types: cancer cells, CD8+ T cells,

FoxP3 regulatory T cells, and myeloid- derived suppressor cells (MDSCs). In turn, cancer cells are subdivided into cancer stem-like cells (CSCs), cancer progenitor cells, and cancer senescent cells; CD8+ cytotoxic T lymphocytes (CTLs) are subdivided into effector, cytotoxic, and exhausted T cell. Cellular agents and cell-cell interactions are governed by defined rules as explained in the following sections. The concentration of molecular agents, mainly cytokines, is described by Partial Differential Equations (PDEs) that are solved numerically. Soluble factors considered include cytokines CCL2, IL-2, IFNγ, enzyme Arg-I, and a signaling molecule NO. All immune-cancer interaction rules are based on published oncology literature; details can be found in recent reviews (Groth et al., 2019; Topalian et al., 2020).

2.1.3 ABM environment

Due to computational limitations, it is not feasible or necessary to track all cells within a tumor beyond a certain size (e.g. > 10^{11} cells). Therefore, we only simulate tumor dynamics within one or several regions of interest (ROI) that can be placed at any tumor locations, e.g. at the invasive front or tumor core. The goal of the present study is to demonstrate the feasibility and general features of the spQSP platform, especially the incorporation of omics data; thus, we did not make an effort to expand the size of the ROI to the limits of available computing power. In this study, we choose $1 \times 1 \times 1$ mm^3 as our ROI, but the volume can vary based on computational power and can be increased several folds. Assuming the diameter of cancer cell is 20 microns, we set the volume of each voxel to be 20x20x20 microns in our simulated volume. Therefore, our ROI contains 50x50x50 voxels. Since each voxel holds one cancer cell, the maximum number of cancer cells in the simulated volume is 125,000. We allow eight (one) T cells to exist in the same voxel without (with) the cancer cell presence. All cells can only move to the six directly adjacent voxels (also known as von Neumann neighborhood), whereas cells

can interact with cells in the Moore neighborhood (26 surrounding voxels)(Gong et al., 2017). To represent tumor vasculature, the entry points of recruited T cell are randomly allocated in the ROI when the model is initialized. The abundance of entry points can be varied by changing vascular density in the model. The tumor vascular density is determined from the experimental data (Stamatelos et al., 2014, 2019) .

Cancer cell

The cancer cell differentiation mechanism is adopted from Norton et al.(Norton et al., 2018). Each cancer cell has three states: cancer stem-like cell (CSC), progenitor cell, and senescent cell. CSCs can either symmetrically divide into two daughter CSCs or asymmetrically divide into one CSC and one progenitor cell with a defined probability. CSCs have unlimited rounds of division. Progenitor cells have limited rounds of division before turning into senescent cells, and their daughter cells are only progenitor cells. Senescent cells cannot divide and will eventually die with defined death rate. All cancer cell related parameters (reproduction rate, death rate, etc.) are defined in the QSP module.

CD8+ T cell

CD8+ T cells has three distinct states in this model: effector, cytotoxic, and exhausted. All CD8+ T cells recruited from the central compartment are effector T cell. Effector T cells are further activated to cytotoxic state upon encountering cancer cells. Cytotoxic T cell can release IFNγ and IL-2 to the surrounding spaces. IFNγ induces PD-L1 expression on all cells. The PD-L1 expression on a specific cell is determined by its surrounding IFNγ concentration, the relationship governed by a Hill function. IL-2 promotes CD8+ T cell expansion in the tumor. If cytotoxic T cells are exposed to sufficient concentration of IL-2, they start limited cycles of

divisions. CD8+ T cells can be exhausted by surrounding PD-L1 since all CD8+ T cells are assumed to express PD-1. Adjacent FoxP3+ regulatory T cells (Treg) can also exhaust CD8+ T cells which can no longer kill cancer cells and die with defined rate.

FoxP3+ regulatory T cell (Treg)

Treg recruitment mechanism is identical to CD8+ T cell and they share the same entry points. Treg cells can exhaust CD8+ T cells. Both exhaustion rate and Treg death rate are determined by parameters in the QSP model.

MDSC

MDSC recruitment mechanism resembles that of other immune cells. MDSCs secrete chemokine (C-C motif) ligand 2 (CCL2), Nitric Oxide (NO), and Arginase 1 (Arg-I). CCL2 facilitates recruiting MDSC; NO reduces CD8+ T cell killing capacity; and Arg-I promotes Treg reproduction. Secretion rate, diffusion rate, and degradation rate for all cytokines are determined by experimental data and provided in the supplemental parameter files(Dutta et al., 2018; Francis & Palsson, 1997; Hakim et al., 1996; B. Huang et al., 2007; Y. Ma et al., 2005; Schimke, 1964; Schweighofer & Ferriol, 2000; Serafini et al., 2008; Tanimoto et al., 2008).

2.1.4 QSP-ABM coupling

The spQSP model extends the QSP model by adding a spatially resolved, fine-grained ABM model; henceforth the QSP and ABM are sometimes referred to as modules to reflect that they are parts of the integrated spQSP model. The high granularity of ABM model where discrete cancer and immune cells of different type are spatially resolved and whose temporal behavior is followed, creates heterogeneous tumor microenvironment that resembles tumor in

patients. However, single cell RNA sequencing data we use in this study have no spatial resolution, thus we randomly initialize cancer cells at the bottom corner of the simulated volume. Both QSP and ABM modules are written in C++ language. To couple QSP module with ABM, the following procedure was taken. We converted the QSP module reported in system biology markup language (SBML) in Wang et al. with a few modifications mentioned above to C++ classes(Wang et al., 2020). Then the ODE system of the QSP module is solved using SUNDIAL CVODE package(Cohen & Hindmarsh, 1996). Since the ABM module represents a portion of the tumor in the QSP module, we use equations and parameters in the QSP module to determine the mechanisms in the ABM module. Finally, the shared information between the ABM and QSP modules is handled by scaling variables in the QSP module**.**

In the QSP module, cancer cells have only one state, and the dynamics is governed by one growth term and multiple death terms, including immune cell killing rate and natural death rate. In contrast, in the ABM module, the cancer cells are differentiated into cancer stem-like cells, progenitor cells, and senescent cells, and rules are adapted from our previous models(Gong et al., 2017; Norton et al., 2018). Cancer stem-like cells have unlimited number of division cycles with a rate r_s. The probability of asymmetric division is k, generating one daughter progenitor cell and one daughter stem-like cell. The probability of symmetric division is 1-k, generating two daughter stem-like cells. Progenitor cells, with limited number of divisions (*dmax*), divide at a rate r_p. The parent cells become senescent after *dmax* cycles of division. Senescent cells cannot proliferate and have a fractional death rate of μ. To connect QSP and ABM cancer growth, we built an ODE version of the ABM rules for cancer cell growth dynamics for comparison purpose. Here S_c, P_i and S_n denote cancer stem-like cell, progenitor cell after i divisions, and senescent cell, respectively.

$$\frac{dS_c}{dt} = r_s(1-k)S_c \qquad \text{(Eq. 1)}$$

$$\frac{dP_1}{dt} = r_s k S_c - r_p P_1 \qquad \text{(Eq. 2)}$$

$$\frac{dP_i}{dt} = 2r_p P_{i-1} - r_p P_i \quad for\ 2 \le i \le dmax \quad \text{(Eq. 3)}$$

$$\frac{dS_n}{dt} = 2r_p P_{dmax} - \mu S_n \qquad \text{(Eq. 4)}$$

Combining equations (1) and (2):

$$\frac{d}{dt}(P_1 - pS_c) = -r_p(P_1 - pS_c) \qquad \text{(Eq. 5)}$$

where

$$p = \frac{kr_s}{r_s(1-k) + r_p}$$

As tumor volume increases, $(pS_c - P_1)$ approaches 0. The same relationship is applicable to other cancer cell types, and the system asymptotically approaches a stable state where all cancer species grow with same rate r^*. The ratio between each pair of cancer cell species asymptomatically approaches the constant r^*:

$$r^* = r_s(1-k)$$

$$\frac{P_1(t)}{S_c(t)} = \frac{kr_s}{r^* + r_p} = l_0 \qquad \text{(Eq. 6)}$$

$$\frac{P_i(t)}{P_{i-1}(t)} = \frac{2r_p}{r^* + r_p} = l_1, \;\; 1 < i \leq dmax \quad \text{(Eq. 7)}$$

$$\frac{S_n(t)}{P_{dmax}(t)} = \frac{2r_p}{r^* + \mu} = l_2 \quad \text{(Eq. 8)}$$

As all cancer cell species' growth rates approach constant r^*, the growth rate equals cancer cell growth rate from QSP module, which is defined in the QSP parameter file. Since r^* can be expressed as a function of k and r_s, when k is set, the growth rate of CSC becomes $r_s = \frac{r^*}{1-k}$, and r_p and μ can be set independently.

Based on results from Eq. 6-8, at steady state, the ratio between any pair of cancer cell species stays the same as tumor is expanding. We then calculate the fraction of each cancer cell species among total cancer cells:

Species	Fraction
S_c	$\frac{1}{q}$
P_i	$\frac{p l_1^{i-1}}{q}$
S_n	$\frac{p l_1^{dmax-1} l_2}{q}$

Table 2: At steady state, fraction of cancer cells grouped by cancer cell type. S_c: Stem-like cancer cell; P_i: Progenitor cancer cell at i^{th} division cycle. S_n: Senescent cancer cell

where $q = 1 + p\frac{l_1^{dmax}-1}{l_1-1} + p l_1^{dmax-1} l_2$

Modifier function of PD-1–PD-LY interaction (Y=1 or 2)

We assume all CD8+ T cell express PD-1 and all cancer cells express PD-L1; this assumption can be readily changed to fit experimental data where available. Our model represents PD-L1 and PD-1 interactions in multiple ways. The model takes the number of PD-1—PD-L1 bonds in the immune synapse as input to the following Hill function:

$$H_{PD1}(X,n) = \frac{(\frac{X}{K\_C1\_PDLY\_Teff\_PD1})^n}{1 + (\frac{X}{K\_C1\_PDLY\_Teff\_PD1})^n} \qquad \text{(Eq. 9)}$$

where Y = 1,2 and $X = C\_PDL1\_Teff\_PD1 + C\_PDL2\_Teff\_PD1$, which is the total number of PD-1 – PD-LY bonds between CD8+ T cell and cancer cell (*Tum* denotes tumor).

The number of PD-1 molecules in the immune synapse can be calculated as:

$$PD1\_syn\_tol = Teff\_PD1\_total \cdot A\_syn/A\_T \quad \text{(Eq. 10)}$$

Total number of PD-L1 molecules involved in the immune synapse can be calculated as:

$$PDL1\_syn\_tot\_max = C\_PDL1\_tot \cdot A\_syn/A\_C \; PDL1\_syn\_tot$$

$$PDL1\_syn\_tot = PDL1\_syn\_tot\_max \cdot H \quad \text{(Eq. 11)}$$

Here, *H* is the Hill function for PD-L1 binding.

In the current version of the ABM, expression of PD-L2 is not accounted for; thus, for consistency we also ignore PD-L2 in the QSP model. This and other simplifying assumptions can be relaxed in subsequent versions of the model. Assuming immune synapse reaches equilibrium

$$PD1\_PDL1 = PD1\_syn \cdot PDL1\_syn \cdot k_1$$

$$PD1\_Nivo\_syn = PD1\_syn * Nivo \cdot k_2$$

$$PD1\_Nivo\_PD1\_syn = PD1\_Nivo\_syn \cdot PD1\_syn \cdot k_3$$

$$PD1\_PDL1 + PD1\_syn + PD1\_(Nivo\_syn\ ) + 2 \cdot PD1\_Nivo\_PD1\_syn = \ PD1\_syn\_tot\ = T_1$$

$$PD1\_PDL1 + PDL1\_syn = \ PDL1\_syn\_tot\ = T_2$$

where

$$k_1 = \frac{k\_on\_PD1\_PDL1}{k\_off\_PD1\_PDL1\ * A\_syn}$$

$$k_2 = \frac{2 * k\_on\_Nivo}{k\_off\_Nivo * gamma\_T\_nivo}$$

$$k_3 = \frac{Chi\_PD1\_nivo * kon\_PD1\_nivo}{2 * koff\_PD1\_nivo}$$

Here Chi_PD1_nivo is the antibody cross-arm binding efficiency, and $gamma\_T\_nivo$ is the volume fraction available to nivolumab.

Let PD-L1 – PD-1 = *X* and x = X/T_2. We rewrite the equation as:

$$x^3 - \left(2 + \frac{1}{k_1 T_2} + \frac{T_1}{T_2} + \frac{Nivo * k_2}{k_1 T_2}\left(1 - \frac{2k_3}{k_1}\right)\right)x^2 + \left(1 + \frac{1}{k_1 T_2} + \frac{2T_1}{T_2} + \frac{Nivo * k_2}{k_1 T_2}\right)x - \frac{T_1}{T_2} = 0 \quad \text{(Eq. 12)}$$

In our model, Eq. 12 is solved respect to *x* using Newton–Raphson method with initial guessing point $x_0 = 0$. Then the total number of PD-L1 – PD-1 bonds, which equals to *xT2*, during immune synapse is calculated dynamically during simulation when each CD8+ T cell interacts with cancer cells. It can be shown that for the parameters of the problem the roots of the equation are real, and we choose the root in the interval 0<x<1.

CD8+ T cell recruitment, expansion, and death

In the QSP module, the CD8+ T cell recruitment is defined as

$$\frac{dT_A}{dt} = q_{T_{A,tumor\ in}} \cdot V_T \cdot T_{A,central} \quad \text{(Eq. 13)}$$

where T_A is the number of CD8+ effector T cells with TCR aligned with antigen A being recruited into the tumor at each time step, V_T is the tumor volume, $T_{A,\ central}$ is the number of CD8+ effector T cell with TCR aligned with antigen A in the central compartment, and $q_{TA,tumor\ in}$ is the rate of CD8+ effector T cell with TCR aligned with antigen A transport into the tumor compartment. Therefore, in the ABM module, the probability of recruiting CD8+ T cell is defined as:

$$p_{T_A,recruited} = T_{A,\ central}\, k_{rec,effector} \quad \text{(Eq. 14)}$$

$$k_{rec,effector} = \frac{q_{T_{A,tumor\ in}} \cdot \Delta t \cdot site\_per\_port}{w \cdot \rho_{adhesion}}$$

Here, Δt is the time per time step, *site_per_port* is number of adhesion sites per port voxel, w is the weight of the QSP model contribution to the spQSP model, and $\rho_{adhesion}$ is the total adhesion site density on tumor vasculature.

In ABM module CD8+ T cell expands upon its activation by the adjacent cancer cell. Each CD8+ T cell divides every d_{T_CD8} hours deterministically. Each CD8+ T cell is limited to n_{T_CD8} divisions before becoming senescent. The lifetime of CD8+ cell is normally distributed with mean μ_{T_CD8} and standard deviation σ_{T_CD8}. All parameters are provided in the supplement.

CD8+ T cell killing of cancer cells

In the QSP module, the CD8+ T cell killing rate is defined as:

$$\frac{dC}{dt} = -k\_C\_death\_by\_T \cdot \frac{T_{CD8}}{C + Tcell + cell}(1 - H_{PD1})\left(1 - H_{MDSC,c}\right)C \quad \text{(Eq. 15)}$$

To translate that equation to the ABM module, the probability of a cancer cell killing by adjacent CD8+ T cell is calculated as:

$$p_{kill} = \ 1 - e^{-\Delta t \cdot \alpha_{c,CD8}}$$

where Δt is the length of each time step, and $\alpha_{c,CD8}$ is defined as:

$$\alpha_{c,CD8} = k\_C\_death\_by\_T \ \cdot \frac{N_{CD8}}{N_c \ + \ N_{tcell} + N_{cell}} (1 - H_{PD1})\left(1 - H_{MDSC,c}\right)$$

$\frac{N_{CD8}}{N_{c1} + N_{tcell} + N_{cell}}$ is the fraction of cytotoxic T cells among all cells in the Moore neighborhood of the target cancer cell.

CD8+ T cell exhaustion

CD8+ T cell can be exhausted by two distinct mechanisms in both QSP and ABM module.

Exhaustion by PD1 - PD-L1 interaction:

In the QSP module, the rate of CD8+ T cell being exhausted by PD1 - PD-L1 interaction is:

$$\frac{dT_{CD8}}{dt} = - T_{CD8} * \ k_{T_{CD8}\_by\_C} \cdot \ \frac{C}{C \ + Tcell + cell} \cdot H_{PD1}(X, 1) \quad \text{(Eq. 16)}$$

where *cell* is the counts of cells other than T cell or cancer cell, and $\frac{C}{C + Tcell + cell}$ is the fraction of cancer cells in the tumor. In the ABM module the probability of single CD8+ T cell being exhausted by PD1 - PD-L1 interaction is:

$$p_{exhaust,PDL1} = 1 - e^{-\Delta t \cdot k\_Teff\_death\_by\_C \cdot H_{PD1}(X,1)) * q\_c} \ = 1 - B_{PDL1}{}^{H_{PD1}(X,1) q\_c} \quad \text{(Eq. 17)}$$

here, $B_{PDL1} = e^{-\Delta t \cdot k\_Teff\_death\_by\_C}$, and q_c is the fraction of cancer cells among all cells in

the Moore neighborhood of the target CD8+ T cell. Since we assume all cancer cells express PD-L1 in the ABM module, *q_c* equals to 1.

Exhaustion by Treg:

In the QSP module, the rate of CD8+ T cell being exhausted by Treg is:

$$\frac{dT_{CD8}}{dt} = -T_{CD8} * k_{T_{CD8}\_by\_Treg} \cdot \frac{Treg}{C + Tcell + cell} * (1 + H_{PD1}) \quad \text{(Eq. 18)}$$

In the ABM module the probability of single CD8+ T cell being exhausted by Treg is:

$$p_{exhaust,Treg} = 1 - e^{-\Delta t * k_{T\_CD8\_by\_Treg} * (1 + H_{PD1}) * q\_treg} \quad \text{(Eq. 19)}$$

Here *q_treg* is the fraction of Tregs in the Moore neighborhood of targeted CD8+ T cell.

Treg recruitment, expansion and death

In the QSP module, the recruitment rate is defined as:

$$\frac{dT_{reg}}{dt} = q_{Treg,T,in} V_T T_{reg,C} \left(1 - \frac{T_{reg}}{T_{reg,max} V_T}\right) \quad \text{(Eq. 20)}$$

where $q_{Treg,T,in}$ is the rate of Treg transport into the tumor compartment, and $T_{reg,max}$ is the maximum number of Treg cells in the tumor compartment.

The expansion of Treg is defined as:

$$\frac{dT_{reg}}{dt} = k_{Treg,exp} T_{reg} \left(1 - \frac{T_{reg}}{T_{reg,max} V_T}\right) \frac{ArgI}{EC50_{ArgI,Treg} + ArgI} = R_{Treg,exp} \quad \text{(Eq. 21)}$$

where $k_{Treg,exp}$ is the rate of Treg expansion induced by Arg-I, $EC50_{ArgI,Treg}$ is half-maximal Arg-I level of Treg expansion.

Since the tumor volume is not clearly defined in the ABM module (only one or several ROIs are considered), we substitute $V_T\left(1-\frac{T_{reg}}{T_{reg,max}V_T}\right)$ with $\frac{site\_per\_port}{w\cdot\rho_{adhesion}}$. The recruitment mechanism is similar to CD8+ T cell recruitment

$$p_{Treg,recruited} = T_{reg,central}\frac{q_{T_{reg,tumor\ in}}\cdot\Delta t\cdot site\_per\_port}{w\cdot\rho_{adhesion}} \quad \text{(Eq. 22)}$$

$T_{reg,\ central}$ is the number of Treg in the central compartment, and $q_{Treg,tumor,in}$ is the rate of Treg transport into the tumor compartment. Additionally, in the ABM module, the time for expansion is inversely proportional to $\frac{R_{Treg,exp}\Delta t}{T_{reg}}$. The lifetime of Treg cell is normally distributed with mean μ_{Treg} and standard deviation σ_{Treg}. All parameters are provided in the supplement.

MDSC recruitment and death

In the QSP module, MDSCs can be recruited in two ways: baseline recruitment and CCL2 induced recruitment. The baseline recruitment is defined as:

$$\frac{dMDSC}{dt} = k_{MDSC,brec}(MDSC_{max}V_T - MDSC) \quad \text{(Eq. 23)}$$

The MDSC recruitment induced by CCL2 is defined as:

$$\frac{dMDSC}{dt} = k_{MDSC,rec}(MDSC_{max}V_T - MDSC)\frac{CCL2}{EC50_{CCL2,rec}+CCL2} \quad \text{(Eq. 24)}$$

where $k_{MDSC,brec}$ is the baseline of MDSC migration rate into tumor, $k_{MDSC,rec}$ is the normal rate of MDSC recruitment into tumor, $MDSC_{max}V_T$ is the maximum number of MDSC in tumor compartment and $EC50_{CCL2,rec}$ is half-maximal CCL2 level of MDSC recruitment.

To translate such mechanism into the ABM module, the baseline probability of recruiting a MDSC at baseline level is:

$$p_{MDSC,brec} = k_{MDSC,brec} \frac{(MDSC_{max} V_T - MDSC)}{V_T} \cdot \frac{\Delta t \cdot site\_per\_port}{w \cdot \rho_{adhesion}} \quad \text{(Eq. 25)}$$

and probability of recruiting a MDSC induced by CCL2 is:

$$p_{MDSC,rec} = k_{MDSC,rec} \frac{(MDSC_{max} V_T - MDSC)}{V_T} \cdot \frac{\Delta t \cdot \text{site\_per\_port}}{\text{w} \cdot \rho_{\text{adhesion}}} \cdot \frac{CCL2}{EC50_{CCL2,rec} + CCL2} \quad \text{(Eq. 26)}$$

The death rate of MDSC in the QSP module is:

$$\frac{dMDSC}{dt} = -k_{MDSC,death} MDSC \quad \text{(Eq. 27)}$$

where $k_{MDSC,death}$ is the death rate of MDSC, so in the ABM module, the dying probability of a MDSC is:

$$p_{MDSC,death} = 1 - e^{-k_{MDSC,death} \times \Delta t} \quad \text{(Eq. 28)}$$

2.1.5 Integrating QSP and ABM sub-models

The spQSP model simulates dynamic response of four compartments identical to the QSP model, and the ABM module is constructed specifically to represent a spatially-resolved volume in the tumor compartment. A subset (set A) of the species, including cancer cells, CD8+ T cells, Tregs and MDSC, are partially built into the ABM module. We simulate all remaining species in both tumor compartment and other compartments (set Ac) with the ODE system from the QSP model. For the species from set A of the tumor compartment, a portion w_{QSP} is simulated by the QSP module, and the remaining $1 - w_{QSP}$ is represented by the ABM module. Also, information exchange between set A and set Ac species is reflected in the ABM module (Supplemental

Figure 7). For instance, recruiting CD8+ T cells, Treg and MDSCs from the central compartment to the QSP tumor compartment is scaled by w_{QSP}, and central compartment immune cell abundance is subtracted by recruited immune cell in the ABM tumor compartment. Here, the nivolumab concentration in the tumor compartment of the QSP module equals nivolumab concentration in the ABM module. The dead cancer cells in the ABM are tracked so that the number can be added to the tumor-specific antigen species in the QSP module after being multiplied by a scaling factor. We then calculate peptide-MHC abundance on antigen presenting cells (APCs) in the lymph node compartment, which initiates CD8+ T cell priming process.

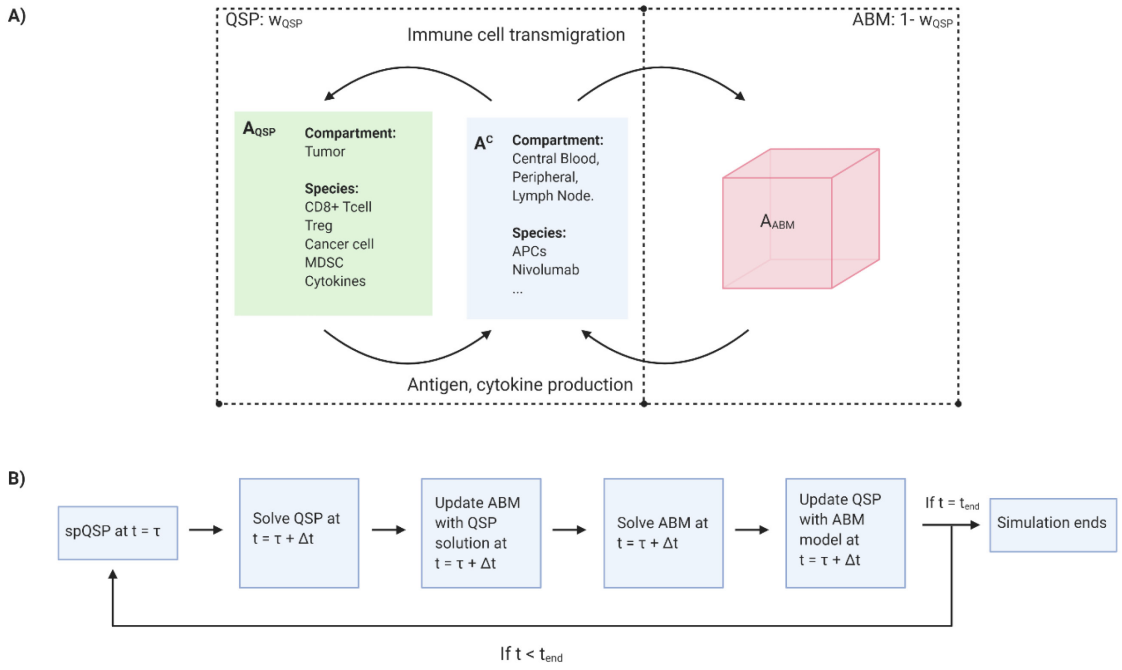

Figure 2: A) Graphical illustration of spQSP model's workflow. Set A_{QSP} are the compartments and species modeled in both QSP and ABM module. Set A_C are the compartments and species only modeled in the QSP module. B) Workflow of synchronizing QSP with ABM module at each time step during the simulation.

Our spQSP platform can include multiple ROIs simultaneously in the ABM module to simulate spatio-temporal dynamics of the tumor microenvironment. Only one ROI is included in this study. The scaling factor *s* of the ROI is calculated based on following equation:

$$s = \frac{1 - w_{QSP}}{w_{QSP}} \times \frac{C_{QSP}}{C_{ABM}} \quad \text{(Eq. 29)}$$

where C_{QSP} and C_{ABM} are the number of cancer cells in the QSP module and ABM module, respectively. We calculate the number of recruited immune cells and the amount of tumor neoantigen produced in the ABM. These quantities are then multiplied by the scaling factor *s* and updated in the QSP module.

Since the QSP and ABM modules are simulated separately, for each timestep Δt, the ABM module is calculated first, with values of the QSP module from the previous timepoint ($t = \tau$). Then the solution of QSP module at time $t = \tau + \Delta t$ is computed. Next, recruited immune cells and generated tumor neoantigens by the ABM module are updated to the QSP module, and both QSP and ABM modules are synchronized at time $t = \tau + \Delta t$.

2.1.6 Transport of soluble factors in ABM

The ABM module has two types of agents: cellular agents and molecular agents. All cellular agents were introduced in the previous section. Molecular agents are cytokines that are produced by cells in the ROI, including INF-γ, IL-2, and CCL2, and molecules NO and Arg-I. The partial differential equation (PDE) governing the concentration of each soluble factor *c* is defined as:

$$\frac{\partial c}{\partial t} = D\nabla^2 c - \mu c + S(x, y, z, t) \quad \text{(Eq. 30)}$$

where *D* is molecular diffusivity, μ is the degradation rate, and *S* is the secretion rate of *c* in

voxel (x, y, z) at time t, and it becomes 0 when there is no source for c.

We use finite volume method implemented in the BioFVM software to solve PDE equations (Ghaffarizadeh et al., 2016). Spatial discretization of the molecular layer matches the voxels in the agent layer. All six surfaces of the simulated parallelepiped (or cubic) volume follow no-flux boundary conditions. When a soluble factor is released by a cell, a source of the factor is created at the location corresponding to the center of the cell's voxel. When the cell migrates to other voxels in the volume, the source moves along with the cell agent to the center of the target voxel.

2.2 Genomic Data Availability and Neoantigen Identification

To identify tumor neoantigens and their expression in each cancer cell, we downloaded TNBC single cell RNA-seq data and WES from Chung et al.(Chung et al., 2017), available in the NCBI Gene Expression Omnibus database under the accession code GSE75688. Briefly, the WES data were used to define neoantigens following the steps outlined below. Then the single-cell RNA-seq data from the tumor cells were used to quantify the heterogeneity of expression of identified neoantigens. The schematic workflow of neoantigen identification is presented in Figure 3. All genes identified as neoantigen genes from this pipeline were filtered for inclusion in TSNAdb, a database that stores all immunogenic mutations from The Cancer Genome Atlas (TCGA) and the immune response was confirmed by Immune Epitope Database (IEDB) (Wu et al., 2018). This analysis yields patient-specific estimates of neoantigen expression, able to model the heterogeneity of neoantigens within and between tumor cells for that patient.

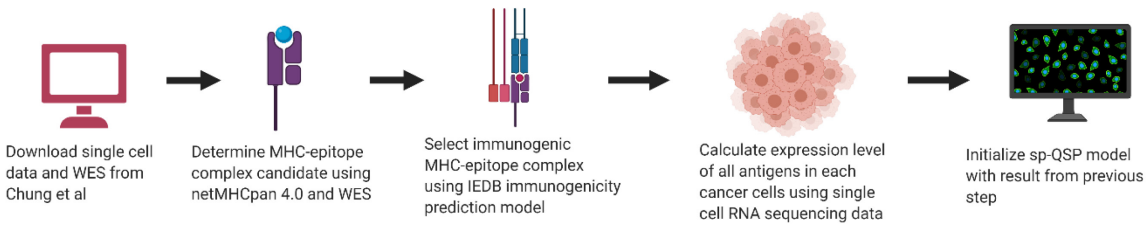

Figure 3: Workflow of immunogenic neoantigen identification from single cell RNA-seq of TNBC in Chung et al, including data source, MHC-peptide binding prediction, immunogenicity prediction, neoantigen expression on cancer cell, integration with spQSP model.

2.3 MHC (HLA) Selection

As most immunotherapies restore cytotoxic activity of CD8+ T lymphocytes, our QSP model focuses on the effect of CD8+ T cells. Therefore, we primarily focus on MHC-I binding with epitopes. The raw sequencing data for the WES data were not available, challenging direct MHC estimation. Therefore, to best ensure MHC-I alleles that we selected are expressed across the population, we chose 16 MHC-I alleles that are expressed in more than 5% of the overall population (Table 3) from 1000 Genome HLA frequency Data (Gourraud et al., 2014). Since Chung et al. study was conducted in Korea, we only rank the frequency within Asian population assuming majority patients in the study were Asian.

		East Asian (n = 371 * 2)			
HLA Locus	***Allele***	***Chinese from Beijing, China (n = 90 * 2)***	***Chinese from Denver-Colorado, USA (n = 90 * 2)***	***Chinese from South China (n = 100 * 2)***	***Japanese from Tokyo (n = 91 * 2)***
	A*0201g	30 (16.67%)	15 (8.33%)	20 (10%)	19 (10.44%)
	A*0206g	8 (4.44%)	10 (5.56%)	9 (4.5%)	17 (9.34%)
	A*0207g	4 (2.22%)	17 (9.44%)	30 (15%)	2 (1.1%)
	A*1101g	45 (25%)	52 (28.89%)	52 (26%)	13 (7.14%)
	A*2402g	32 (17.78%)	31 (17.22%)	38 (19%)	68 (37.36%)
	A*3303g	15 (8.33%)	4 (2.22%)	12 (6%)	19 (10.44%)
	B*1301	7 (3.89%)	14 (7.78%)	15 (7.5%)	2 (1.1%)
	B*4001g	22 (12.22%)	28 (15.56%)	41 (20.5%)	9 (4.95%)
	B*4601g	21 (11.67%)	19 (10.56%)	37 (18.5%)	10 (5.49%)

	B*5101g	12 (6.67%)	11 (6.11%)	10 (5%)	14 (7.69%)
	C*0102g	29 (16.11%)	32 (17.78%)	40 (20%)	24 (13.19%)
	C*0303g	11 (6.11%)	8 (4.44%)	16 (8%)	25 (13.74%)
	C*0304	14 (7.78%)	23 (12.78%)	34 (17%)	25 (13.74%)
	C*0602	14 (7.78%)	13 (7.22%)	7 (3.5%)	3 (1.65%)
	C*0702g	30 (16.67%)	37 (20.56%)	46 (23%)	26 (14.29%)
	C*0801g	19 (10.56%)	19 (10.56%)	15 (7.5%)	14 (7.69%)

Table 3: Selected Human Leukocyte Antigen (HLA) for neoantigen peptide binding prediction from Gourraud et al. Each selected HLA allele must be expressed in more than 5% of the overall Asian population. In total, 16 alleles were chosen based on the criteria.

2.4 MHC-I Binding Prediction

Chung et al. WES data contain only single nucleotide polymorphism (SNP), so indels and frameshifts were excluded from forming neoantigens(Chung et al., 2017). We used netMHCpan 4.0, a web tool predicting peptide-MHC affinity based on neural network approach to select MHC-epitopes (Jurtz et al., 2017). The inputs are 16 HLA alleles selected from previous step and 21-mer-peptide with the mutational site at the center, and the output is the MHC-epitope complex predicted by netMHCpan 4.0.

2.5 MHC-epitope Immunogenicity Prediction

To ensure predicted MHC-epitopes complexes are immunogenic, we used IEDB Class I Immunogenicity web tool to predict if MHC-epitopes complexes can elicit immune responses (Calis et al., 2013). Calis et al. uses “immunogenicity score” to quantify strength of immune response elicited by epitopes. Based on experimental data, immunogenic epitopes have average immunogenicity score 0.097 verses non-immunogenic epitopes score 0.01. Therefore, epitopes with immunogenicity score higher than 0.1 are considered immunogenic, and the genes that express the peptide are identified as tumor neoantigens.

2.6 Tumor Neoantigen Expression in Cancer cell and T cell in ABM module

We further use the single-cell RNA-seq data from Chung et al. to model neoantigen

heterogeneity within the tumor cells(Chung et al., 2017). We apply SAVER to the single cell expression profiles to estimate expression profiles in spite of the missing data from the technical dropout in single cell RNA-seq and log transform estimated transcript per million (TPM) values(M. Huang et al., 2018). We use kernel density estimation to approximate the expression distribution of one antigen across all cancer cells within single patient, excluding cells with expression values in the bottom 10% in this estimate to account for dropout. This binary expression value is used as input to the spQSP model, using this simplification of binary tumor neoantigen expression (expressed vs. not expressed) in each cancer cell as input to the model. We use these data to calculate the coefficient of variance (CoV) of neoantigen frequency to quantify tumor neoantigen heterogeneity, expressed as $\frac{\sigma_{antigen/cell}}{\mu_{antigen/cell}}$, where $\sigma_{antigen/cell}$ is the standard deviation of neoantigen frequency, and $\mu_{antigen/cell}$ is the mean of neoantigen frequency. This metric enables us to represent the difference between diverse neoantigen expression within a small subpopulation of tumor cells from uniform neoantigen expression across distinct subclones of cancer cells within the tumor.

The T cell recognition is modified from our previously published model of TNBC(Wang et al., 2020) to pair specific TCRs to neoantigens. We leveraged this new model of T cell recognition to study the impact of tumor cell heterogeneity on patient-specific immunotherapy response. The spQSP model further requires that T cells can recognize each antigen to yield effective T cell killing. Specifically, alignment between the hypervariable loop (CDR3α, CDR3β) and epitopes is required for immune response and killing of cancer cell, thus it is crucial to describe TCR-epitope specificity in our mathematical model (Glanville et al., 2017; Singh et al., 2017). We assume that MHC-epitope (pMHC) and T cell receptor (TCR) on CD8+ T cell has

one-to-one relationship: each TCR can only recognize one and only one epitope, and the graphical illustration is shown in Figure 4.

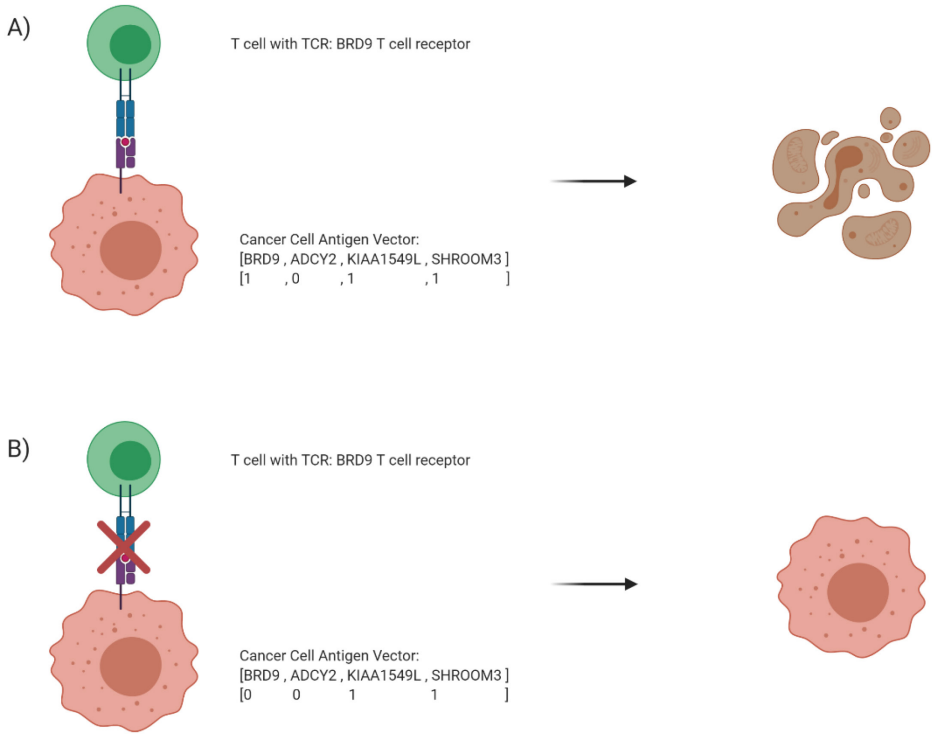

Figure 4: Illustration of TCR specificity in current model. To kill the cancer cell, TCR must match existing antigen of the target cancer cell. A) The TCR antigen alignment leads to cancer cell death. B) The TCR cannot align with any antigen in the cancer cell, hence the cancer cell survives.

2.7 Simulated Digital Pathology Data

To resemble digital pathology data, the spatial result from ABM module is sliced every 0.05 mm in the y direction; therefore, twenty immunofluorescence (IF) panels are generated at each time point. Our simulated IF panels are compared with the multiplexed data in Keren et al. We applied the same metric from Keren et al. -- mixing score, a method quantifying the separation between the immune cells and cancer cells. The mixing score is calculated based on

fraction of immune cells adjacent to cancer cells. We define cell *A* is in contact with the target cell if cell *A* is in the 2D von Neumann neighborhoods (range = 1 pixel)of the target cell (Das, 2011). All patient TME are distinguished between two categories: mixed (mixing score > 0.22) and compartmentalized (mixing score < 0.22).

2.8 Model Initialization and Simulation

Since the number of cancer cells sampled in the scRNA-seq data was low (13 to 28 cancer cells per sample), we use bootstrapping to increase number of cancer cells to 1000 as the initial condition for all simulations. To represent inter-patient variability, a virtual patient cohort is generated by varying a subset of model parameters. Those values are sampled using Latin Hypercube Sampling (LHS) based on estimated distributions. A set of complete model parameters is defined as a virtual patient, and each virtual patient cohort contains one hundred patients in this study. All model parameters are provided in the Supplemental Material. In the model, anti-PD-1 immune checkpoint inhibitor nivolumab at 3mg/kg is administered to every virtual patient via bolus injection every two weeks, and each simulation last for 200 days. The spQSP model is built with C++ language, and all simulations are run on a Linux compute cluster.

2.9 Sensitivity Analysis

To thoroughly investigate the impact of input parameter on tumor progression, including cancer cell counts, immune cell density, and other features, we conduct parameter sensitivity analysis for 18 parameters. The values of analyzed parameters are sampled using Latin Hypercube Sampling (LHS)(Helton & Davis, 2003). We sampled 400 parameter sets based on approximated distribution. Partial Rank Correlation Coefficient (PRCC) is calculated between treatment outcome and input parameters to quantify the sensitivity of each selected parameter(Marino et al., 2008)

3. Results

3.1 Tumor Neoantigen Abundance Impact on Tumor Progression

We adapted our previous parameterization of the spQSP model for TNBC (Wang et al., 2020) to model patient specific-responses to anti-PD-1 (nivolumab) monotherapy using combined WES data and scRNA-seq data of tumor cells from Chung et al. (Chung et al., 2017). This dataset contains 4 total TNBC patients from the 11 total patients sampled (patient 7, 8, 10, and 11, Figure 5) that reflect a range of antigen burdens (Patient 7: 15 neoantigens; Patient 8: 17 neoantigens; Patient 10: 6 neoantigens, and Patient 11: 4 neoantigens in total) and CoV of neoantigen frequency reflective of intra-tumoral heterogeneity of neoantigen expression (Patient 7: 0.140, Patient 8: 0.193, Patient 10: 0.396, Patient 11: 0.142). Therefore, incorporating this dataset into the tumor compartment of the spQSP model enables us to study how tumor neoantigen abundance and heterogeneity influence the immunotherapy efficacy (Figure 6).

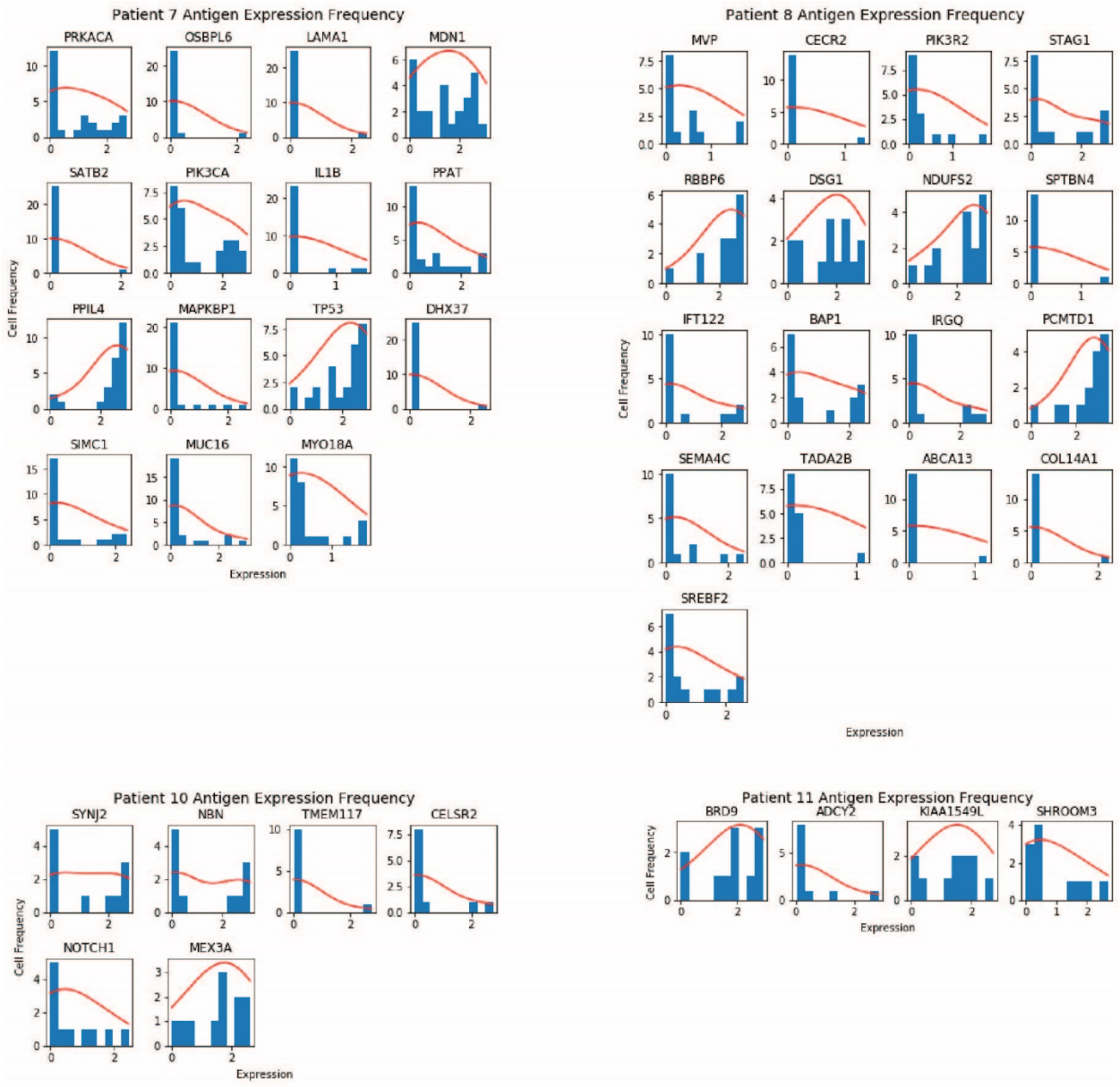

Figure 5: Neoantigen expression frequency (in TPM) for each patient using the single cell sequencing data (shown in blue histogram, Patient 7: 15 neoantigens, Patient 8: 17 neoantigens, Patient 10: 6 neoantigens, Patient 11: 4 neoantigens). Kernel density estimation (shown in red line) is applied to approximate the expression distribution of each identified antigen across all cancer cells within single patient. Neoantigen with expression values in the bottom 10% are excluded in this estimate to account for dropout.

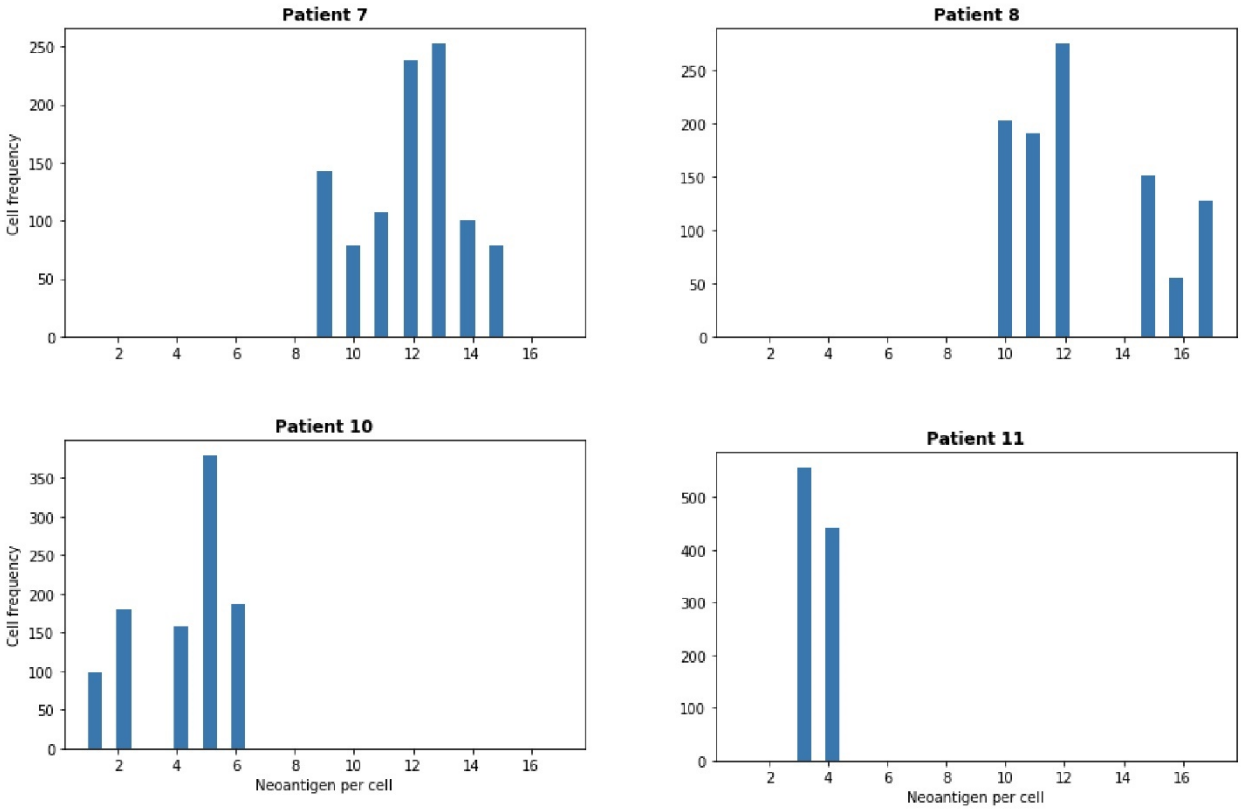

Figure 6: Cell frequency distribution of bootstrapped 1000 cancer cells in ABM at Day 0. X-axis represents number of neoantigens in single cancer cell; y-axis represents cell frequency contains n neoantigens.

Treatments were simulated for 200 days, with tumor progression snapshots taken at Day 0, 30, and end of treatment for all patient samples (Figure 7). Only patients 7 and 8 who had the highest neoantigen burden responded to the nivolumab therapy. Our results qualitatively agree with clinical data suggesting that immunotherapy is more effective in patients with more tumor neoantigens (Goodman et al., 2017; Rizvi et al., 2015; Rooney et al., 2015).

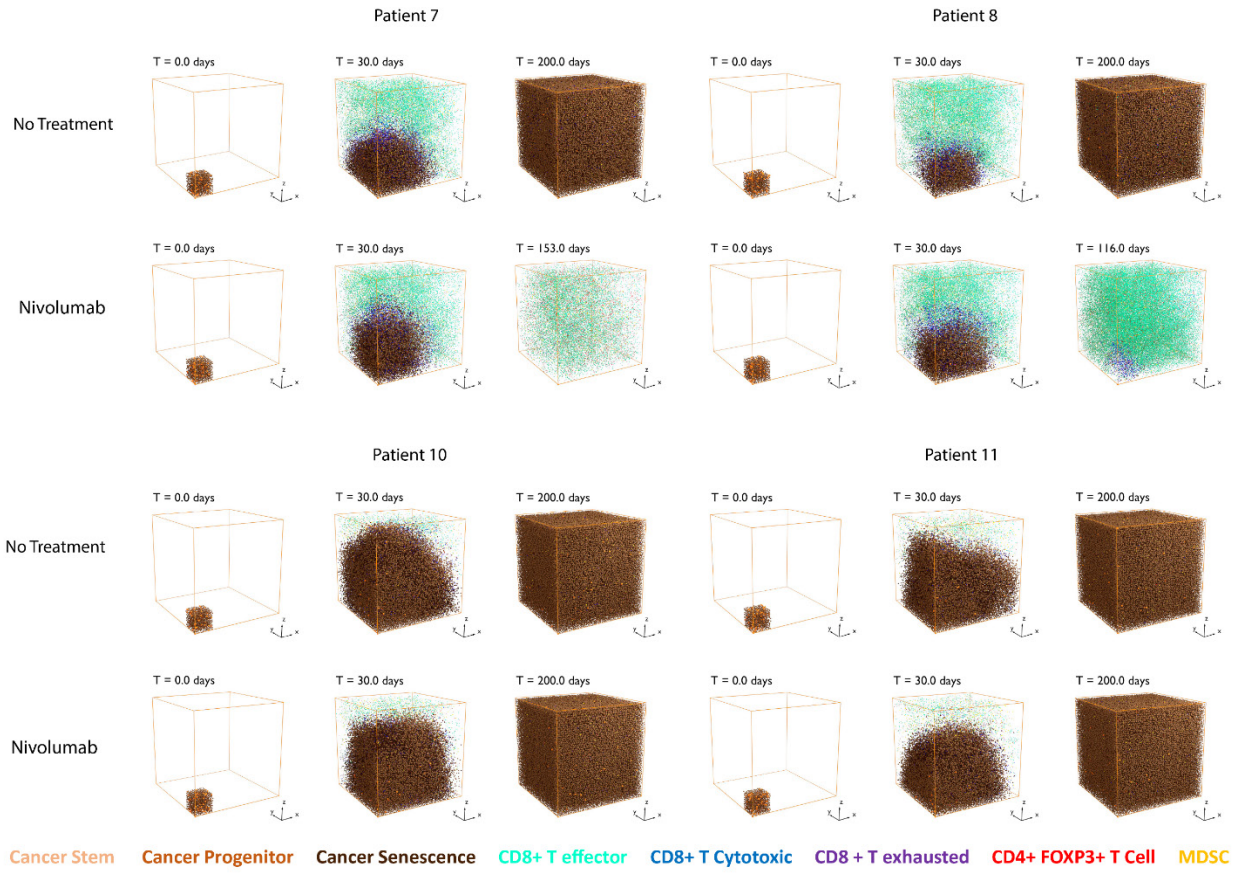

Figure 7: Visualization of the ABM simulation result. Tumor growth is simulated for 200 days total (no treatment vs. nivolumab monotherapy). The dosing regimen for nivolumab is 3mg/kg every 2 weeks starting from day 0. Snapshots are taken at day 0, day 30, and end of simulation (≤ day 200). Light pink: Stem-like cancer cell; Brown: Progenitor cancer cell; Dark Brown: Senescent Cancer cell; Cyan: CD8+ effector T cell; Blue: CD8+ cytotoxic T cell; Purple: Exhausted CD8+ T cell; Red: FoxP3+ T cell; Yellow: MDSC.

In clinical practice, TMB is used as a surrogate to tumor neoantigen as immunogenic neoantigens are more complicated to identify, and cancer genes with higher mutation rate can potentially produce more tumor neoantigens (Fancello et al., 2019). To further verify our findings, four virtual patient cohorts are generated based on each patient's neoantigen profile (400 virtual patients in total). Then, we simulate tumor progressions for all four virtual patient cohorts receiving no treatment vs. nivolumab monotherapy with dosing regimen of 3mg/kg every 2 weeks starting at Day 0 (Figure 8, 9). We define a patient as a "responder" if tumor count is below 1000 cancer cells by the end of the simulation. Among 400 virtual patients who received nivolumab monotherapy 31 (8 %) responded, which is qualitatively consistent with clinical

results(Planes-Laine et al., 2019). Simulated cancer cell counts were reduced significantly only in the two patients with highest neoantigen burden (Patient 7: 12.0% reduction, p-value of 0.0011; Patient 8: 22.7% reduction, p-value of 8.1×10^{-7}; Patient 10: 0.9% reduction, p-value of 0.99; Patient 11: 2.9% reduction, p-value of 0.72; Supplemental Figure S4). This further demonstrates that our model correctly models that patients with more tumor neoantigens potentially have better clinical outcome.

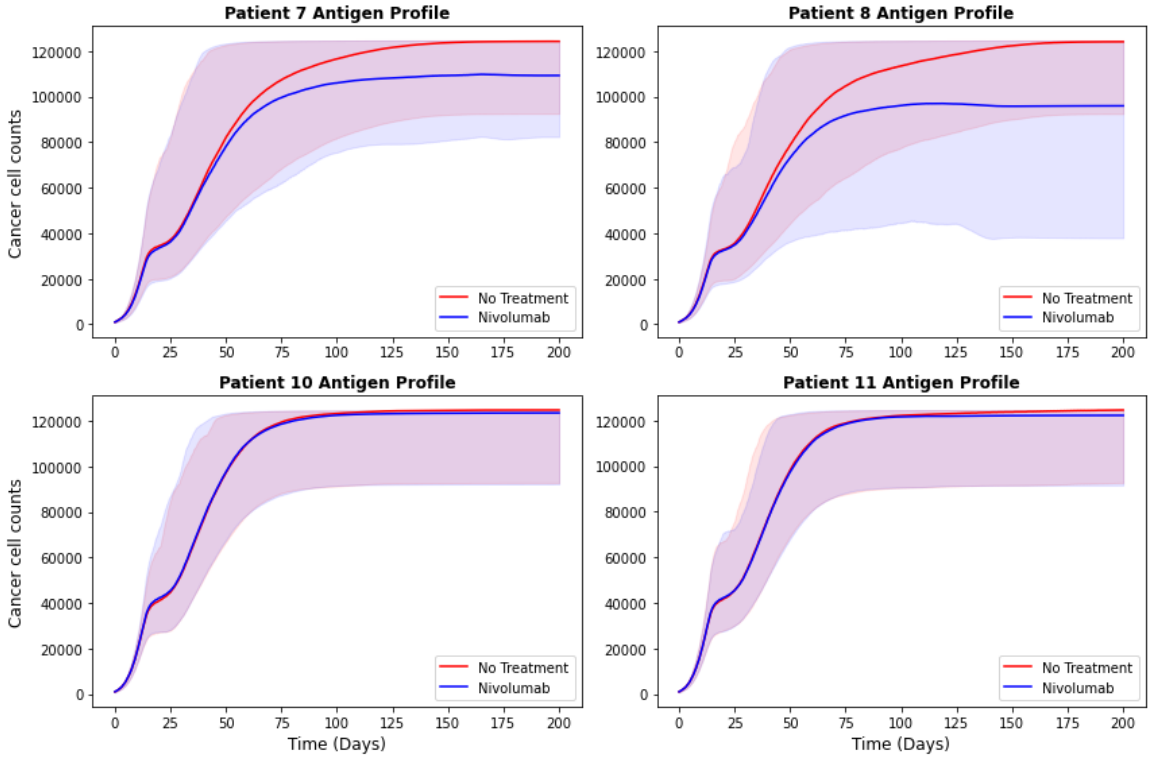

Figure 8: Cancer cell progression (200 days) comparison between no treatment vs. nivolumab monotherapy (n = 100) for each patient's antigen profile, and the parameter ranges are derived from Wang et al. Solid line represents mean cancer cell count, and shaded area represents 80% predicted interval of the mean cancer cell counts.

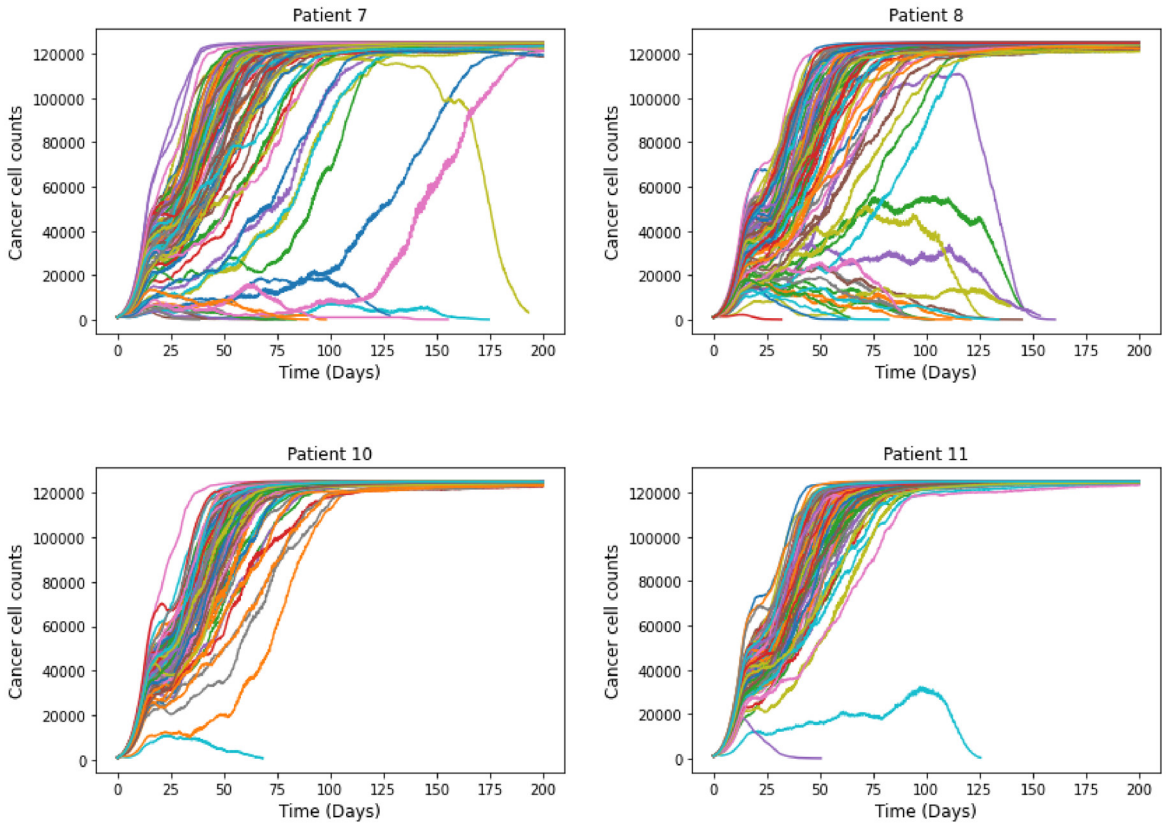

Figure 9: Spider plot of 400 randomly selected virtual patients under four different patient neoantigen profiles.

Next, we use these simulations to further analyze immune biomarkers associated with individual patients. We use simulated cell type abundances to investigate whether clinically established immune biomarkers also have predictive power in our model. All values are taken at day 30 of the simulation to mimic biopsy at early-stage treatments. The density of CD8+ T cells and myeloid-derived suppressor cells (MDSCs) have strong predictive power of differentiating responders and non-responders (Figure 10A, 10B). Somewhat counterintuitively, responders have higher tumor FoxP3+ density (Figure 10C), but this result is also consistent with clinical data(Yeong et al., 2017). Furthermore, the ratio of CD8+ T to FoxP3+ T cells has been regarded as a positive biomarker of response to immunotherapy (Liu et al., 2011). In Figure 10D, our simulations show that CD8+/FoxP3 ratios for patients who responded to nivolumab had 2.14

times of the ratio for non-responders ($p = 3.9 \times 10^{-16}$). Altogether, integration of scRNA-seq data of tumor cells with the spQSP model qualitatively reproduced immune profiles that resemble clinical results and showed that tumor progression could be predicted by conventional biomarkers.

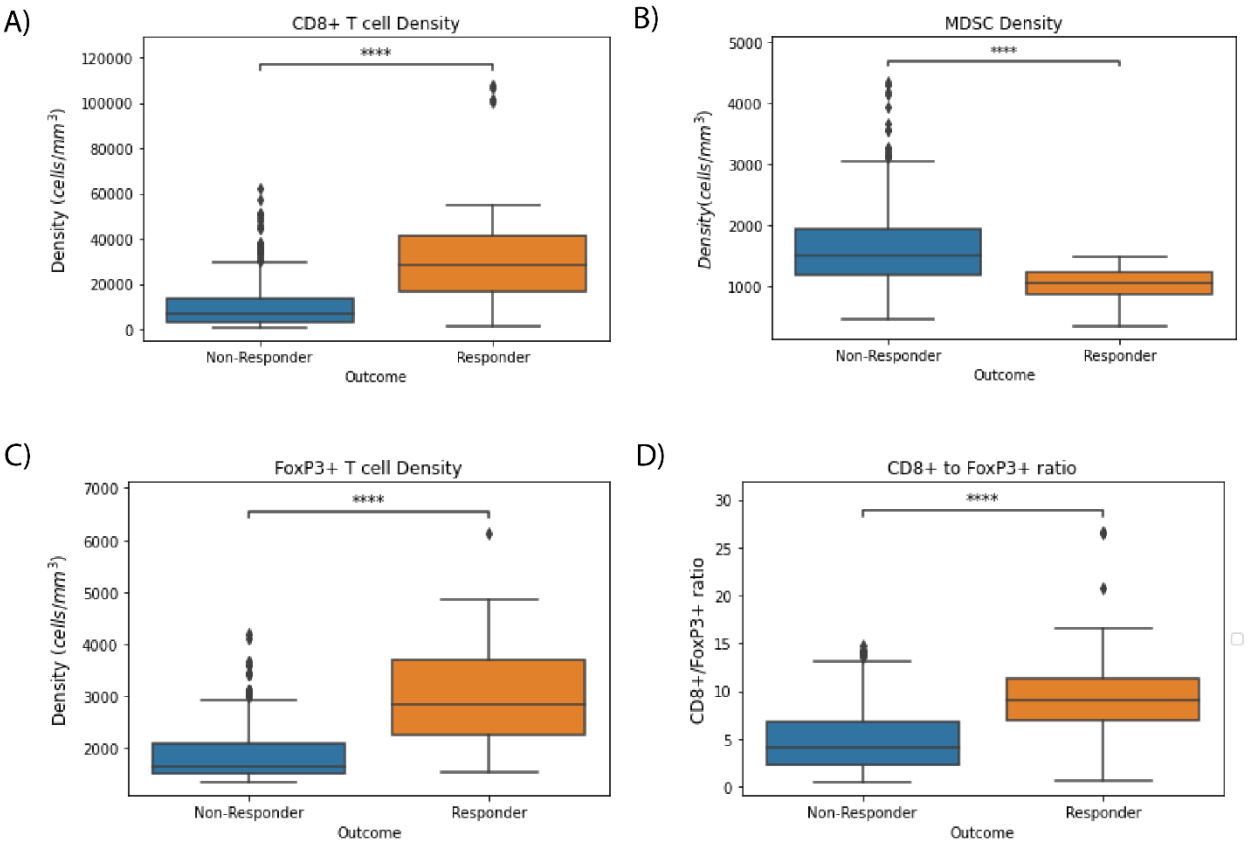

*Figure 10: Immune biomarker comparison between responders and non-responders at Day 30 of the treatment. A) CD8+ effector T cells; B) MDSCs; D) FoxP3+ regulatory T cells; D) CD8+ effector T cell and FoxP3+ regulatory T cell ratio. (Student t-test, ns: 5.00e-02 < p <= 1.00e+00; *: 1.00e-02 < p <= 5.00e-02; **: 1.00e-03 < p <= 1.00e-02; ***: 1.00e-04 < p <= 1.00e-03; ****: p <= 1.00e-04)*

3.2 Tumor Neoantigen Heterogeneity Influence Treatment Outcome

Our simulations demonstrate that Patient 10 has the worse treatment outcome (1%) than Patient 11 (3%) despite the fact that Patient 10 has more tumor neoantigens than Patient 11 (6 and 4, respectively). This observation seems contradictory to the results presented above and

utility of TMB as an immunotherapy biomarker. Given that Patient 10 has the highest CoV of tumor neoantigen, we hypothesize that patients with higher tumor neoantigen heterogeneity have worse prognosis due to a lower probability of T cell recognition of an individual antigen. We test this hypothesis by increases the number of T cell clones in the simulations of Patient 10 and 11 to levels that enable these patients to respond to nivolumab therapy. As we did in the previous section, we sampled two additional virtual patient cohorts under both Patient 10's and 11's neoantigen profiles (200 virtual patients total) and simulate tumor progression under treatment from nivolumab monotherapy for patients from both cohorts. The results show that tumor in Patient 10 acquired immunotherapy resistance at a later timepoint of the treatment than in the original simulations for a lower number of T cells (Fig 11A), whereas tumor in Patient 11 is stably controlled (Figure 11B). On average, tumor in Patient 11 contains 25.7% fewer cancer cells than that in Patient 10 ($p = 6.3 \times 10^{-3}$, Student t-test) (Figure 11H).

To further investigate how higher tumor neoantigen heterogeneity leads to immunotherapy resistance, we focused on the neoantigen composition of cancer cells in the tumor. We found that cancer cells with fewer tumor neoantigens tend to survive throughout the treatment because they are less likely to be killed by CD8+ cytotoxic T cells (Figure 11C - F). Since the cancer cells remaining after treatment as immunotherapy resistant contain fewer tumor neoantigens, T cell diversity also reduces over the course of the treatment (Figure 11G). To summarize, high tumor neoantigen heterogeneity leads to the reduction of abundance of activated CD8+ in the tumor which in turn causes the immunotherapy resistance. This process is better reflected in case of Patient 10. In contrast, since at least 3 neoantigens are expressed in cancer cells in Patient 11, the number of activated CD8+ T cell stays stable. Therefore, the efficacy of nivolumab is preserved. This is in agreement with clinical studies that demonstrated

that higher CD8+ T cell diversity demonstrate superior responses to immunotherapy in NSCLC and mesothelioma (Han et al., 2020; Vroman et al., 2020).

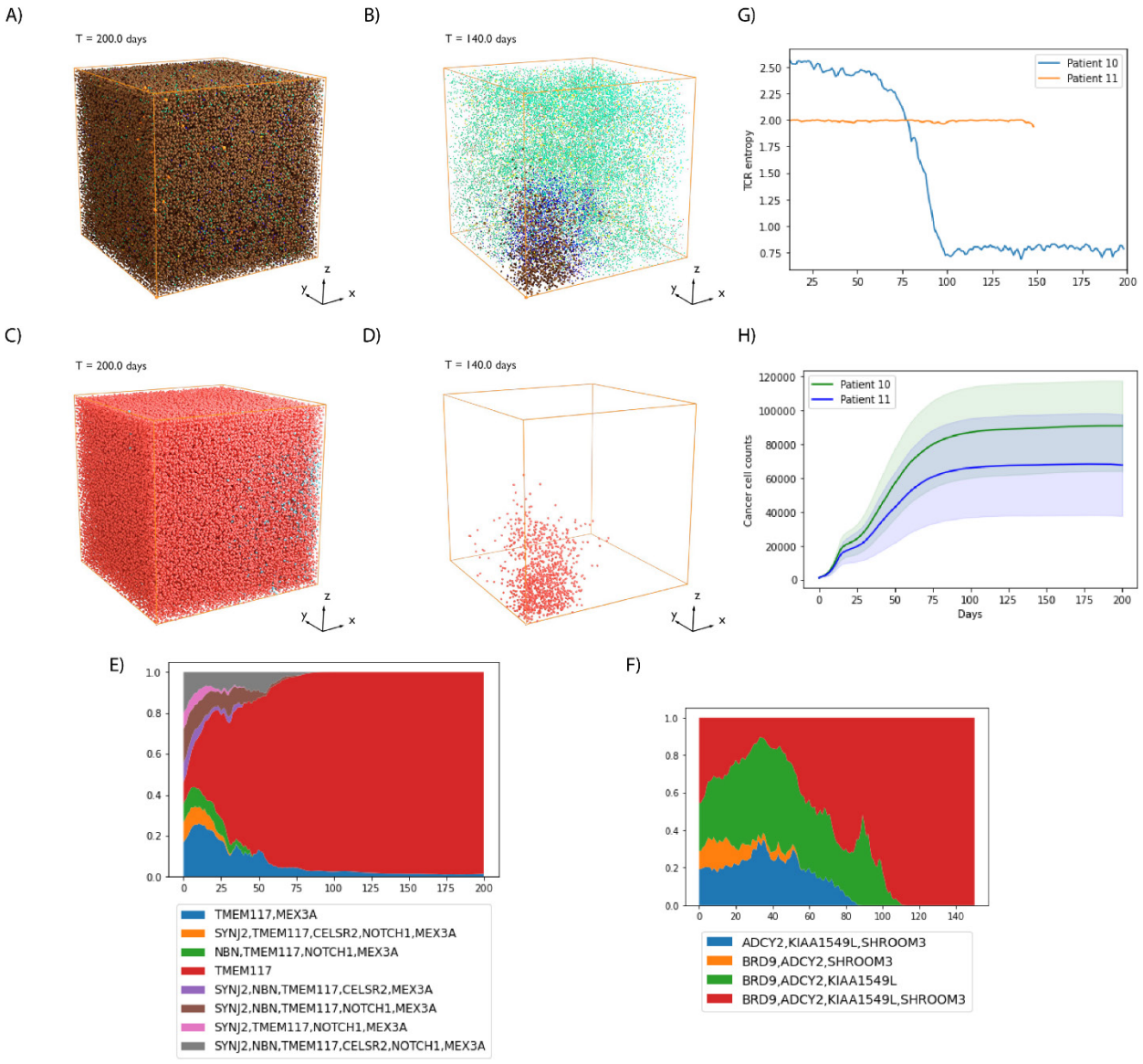

Figure 11: A, B) 3-D visualization of ABM results for Patient 10 and Patient 11 by the end of the treatment, respectively. C, D) Visualization of cancer cells and immune cells for Patient 10 and Patient 11 by the end of the treatment, respectively. Cancer cells are colored by neoantigen clones (same legend for E and F). E, F) Cancer cell composition in the ABM module over the 200-day treatment for Patient 10 and 11, cancer cells are grouped by tumor neoantigen they contain. G) Time-dependent T cell receptor (TCR) entropy over the course of nivolumab treatment. H) Cancer cell progression for all virtual patients using patient 10's and 11's tumor neoantigen profiles under nivolumab over 200 days (n = 100). Solid line represents average cancer cell count, and shaded area represents 80% predicted interval of the mean cancer cell counts.

We explore the simulated post-treatment cancer cell composition of both virtual patient cohorts to reinforce our findings (Figure 12). The average antigen expressed on cancer cell is significantly reduced for Patient 10 (pre-treatment: 4.02, post-treatment: 2.47, $p = 1.45 \times 10^{-12}$, Student t-test), whereas the result is not significant for Patient 11 (pre-treatment: 3.45, post-treatment: 3.35, $p = 0.49$, Student t-test). Our simulations are consistent with Gejman et al. data that diverse neoantigens expression leads to failure of immune-mediated cancer cell elimination(Gejman et al., 2018). Clinical results for NSCLC patients also indicate that high neoantigen heterogeneity negatively impacts treatment outcomes(McGranahan et al., 2016). Our results indicate that tumor neoantigen heterogeneity, which is quantified as CoV, can be regarded as a potential biomarker to predict post-treatment outcome.

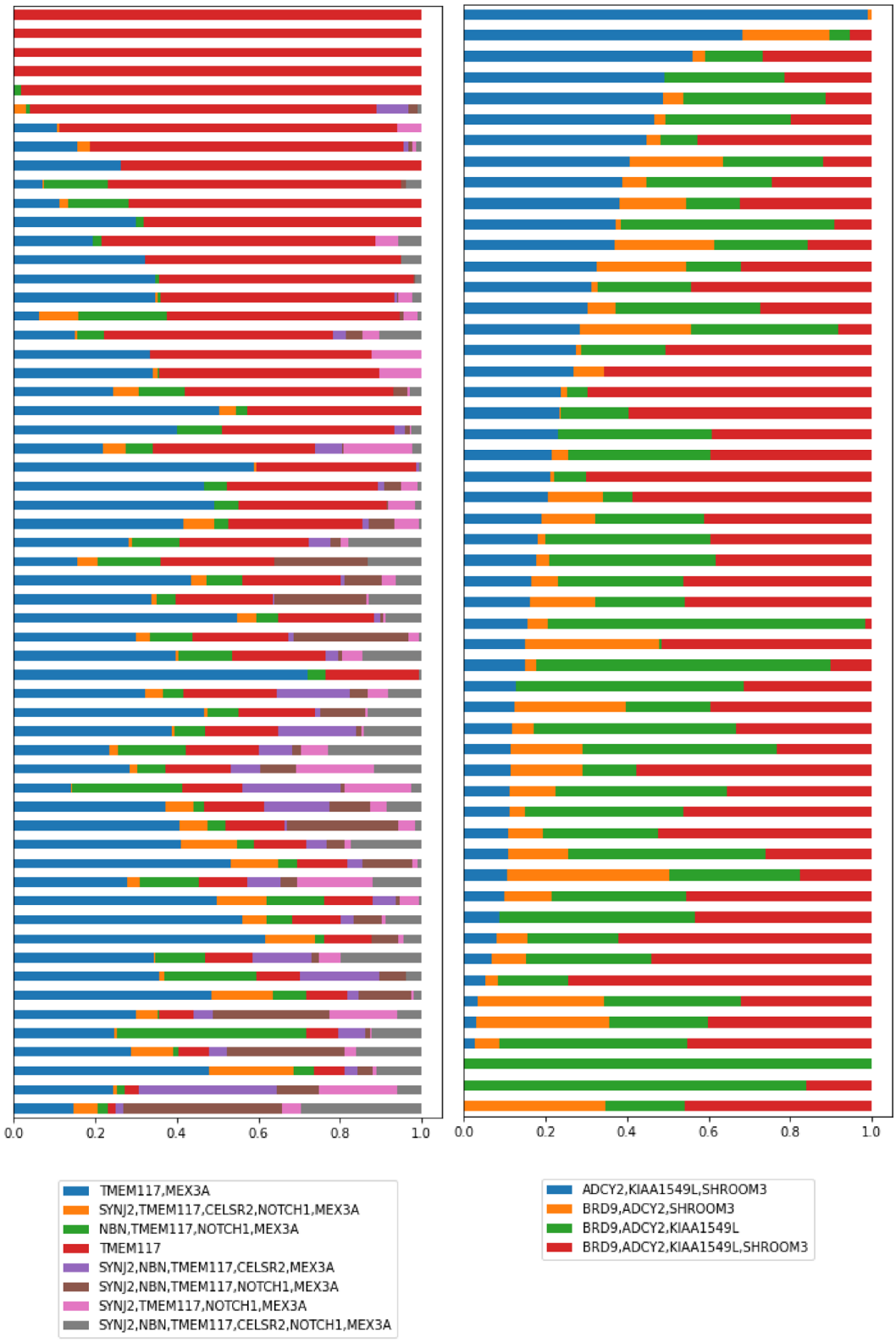

Figure 12: Cancer cell composition at the end of the treatment. Left: 100 simulations for 200 days nivolumab treatment under Patient 10's neoantigen profile. Right: 100 simulations for 200 days nivolumab treatment under Patient 11's neoantigen profile. Cancer cells are grouped by neoantigens they contain.

3.3 Results of simulations resemble spatial clinical data.

While the single cell RNA-sequencing data used to initialize our model is from dissociated cells, and advantage of the spQSP model is its ability to capture the spatial resolution of tumors. Comparing spatial molecular data from digital pathology data with the spatial distribution of cells from the spQSP simulations validate the model. Thus, we qualitatively compare the simulated cell distribution from the ABM module with Keren et al. multiplexed pathology proteomics imaging data from TNBC patients (Keren et al., 2018). The data use multiplexed ion beam imaging quantifying in situ 36 protein expression in 41 TNBC patients. In that study, patients with compartmentalized TME quantified through a mixing ratio between tumor and immune cells exhibited better overall survival rates. To compare our simulations to the structure of response in Keren et al., we calculate tumor mixing score on the simulated spatial distribution of cells on Day 60 and observed consistent results: both Patient 10's samples form mixed tumor (Sample 1 mean mixing score: 0.71, Sample 2 mean mixing score: 0.75, Figure 13 top), and they are predicted to have worse treatment outcome (Das, 2011). In contrast, both samples from Patient 11 are compartmentalized TME (Sample 1 mean mixing score: 0.17, Sample 2 mean mixing score: 0.12, Figure 13 bottom). We hypothesize that in compartmentalized tumors cancer cells' growth is impeded by the immune system. Even though the results from a small sample size with qualitative comparison to the distributions in this larger cohort, these simulations demonstrate that our spQSP model can simulate spatial distributions that qualitatively resemble clinical multiplexed data.

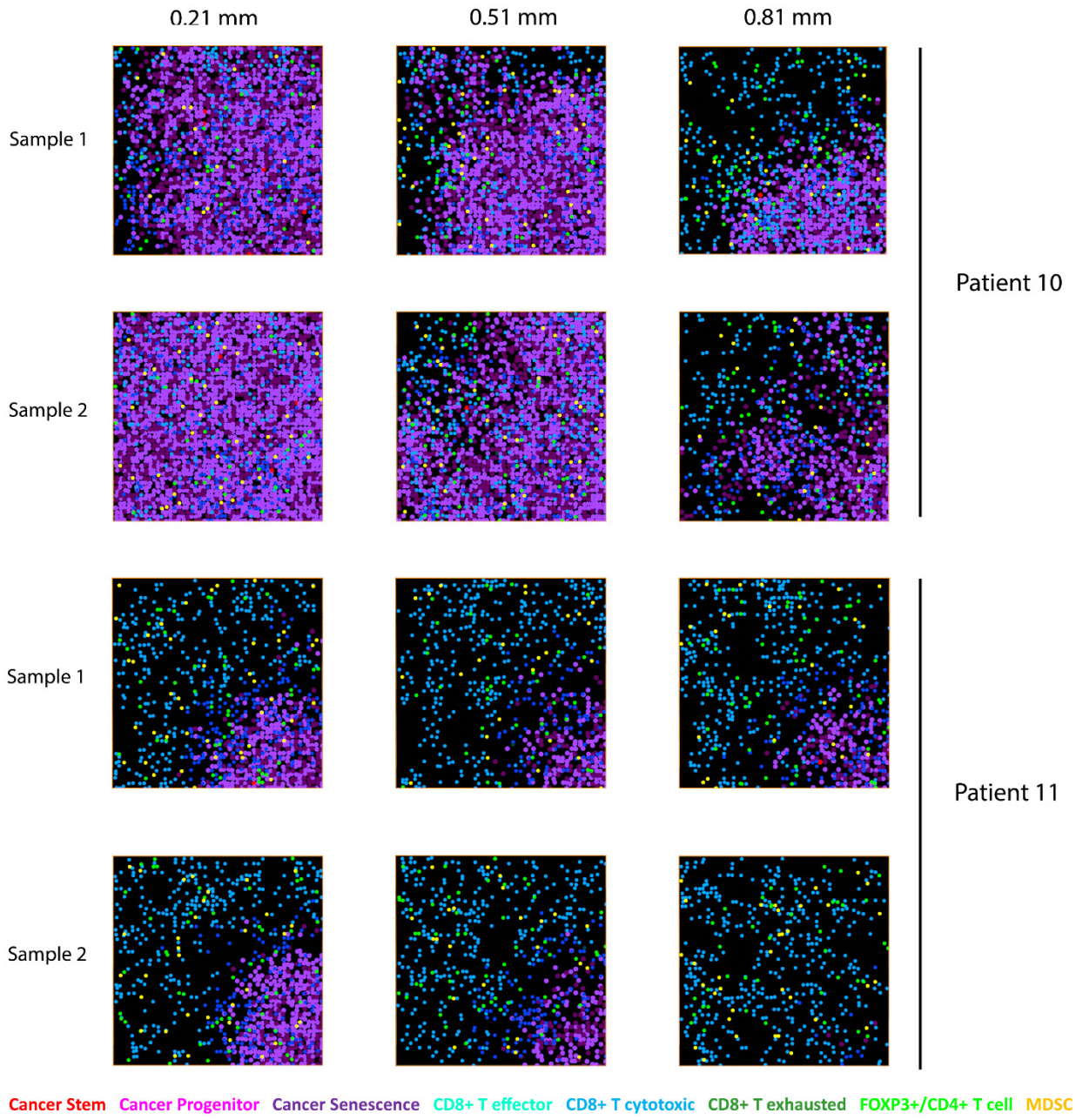

Figure 13: Samples of simulated immunofluorescence (IF) for patient 10 and 11 at Day 60. The mixing score is calculated based on the method from Keren et al (Patient 10: Sample 1 mean mixing score: 0.71, Sample 2 mean mixing score: 0.75, Patient 11: Sample 1 mean mixing score: 0.17, Sample 2 mean mixing score: 0.12). The cross-section of IF is taken along the y-axis at 0.21 mm, 0.51mm, and 0.81 mm. Red: Stem-like cancer cell; Magenta: Progenitor cancer cell; Dark Purple: Senescent Cancer cell; Cyan: CD8+ effector T cell; Light Blue: CD8+ cytotoxic T cell; Dark Green: Exhausted CD8+ T cell; Light Green: FoxP3+ T cell; Yellow: MDSC.

3.4 Sensitivity Analysis

To test the uncertainty of the spQSP model predictions, we performed global sensitivity analysis for 18 input parameters, including Cancer cell growth rate, T cell clone per antigen, PD-L1(2) expression level, etc. Output parameters include counts of post-treatment cancer cells, CD8+ T cells, Treg, and MDSC in both QSP and ABM modules. We used Partial Rank Correlation Coefficient (PRCC) to quantify the uncertainty of input parameters (Figure 14). In general, the output values in the QSP module have very similar sensitivity as output values in the ABM module for the same input parameter. The results are consistent with the notion that the QSP and ABM modules are generally coupled. However, we saw discrepancies for some input parameters that will be discussed in the next section. We found that Cancer cell growth rate, T cell clone per antigen, T cell killing rate, PD-L1 expression level, and Maximum MDSCs have significant impact on post-treatment cancer cell counts, which implies treatment outcomes.

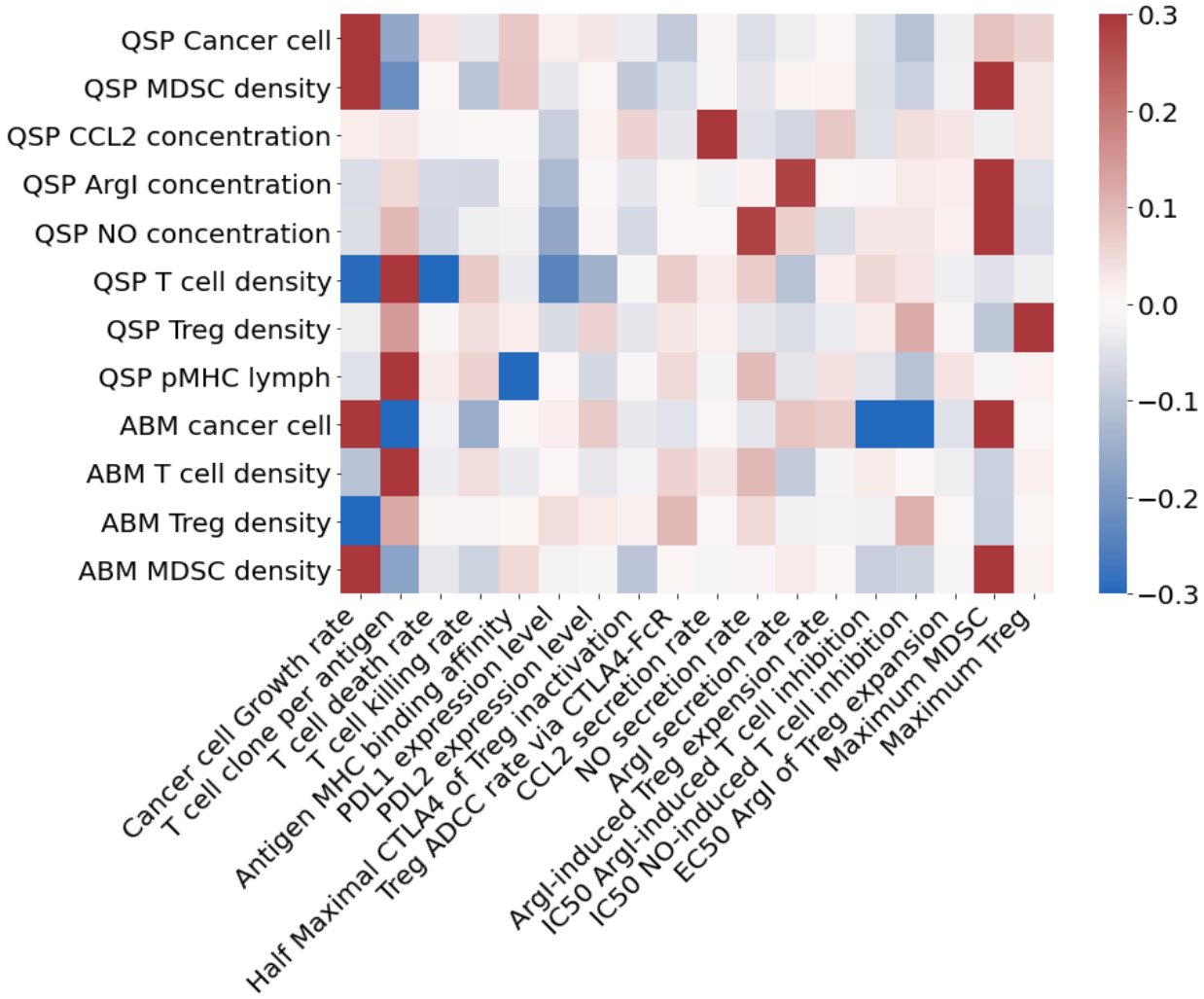

Figure 14: Global sensitivity analysis of 18 parameters sampled by Latin Hypercube Sampling (LHS) method. The Partial Rank Correlation Coefficient (PRCC) between simulated post treatment outcome and input physiological parameters.

4. Discussion and Conclusion

In this study, we investigate how tumor neoantigen burden and heterogeneity impact the efficacy of immunotherapy by incorporating high-throughput sequencing data into a computational spatial spQSP model of immunotherapy response. To enable the integration of high-throughput data, our spatial spQSP model blends multiple mathematical modeling frameworks. First, the QSP module simulates tumor progression at organ and whole patient level with parameters that are specifically defined for TNBC. However, due to the limitation of the compartmental QSP model, spatial heterogeneity is not represented. The addition of the ABM module of the tumor and its microenvironment allows us to overcome this limitation. The discretized agents allow us to further differentiate phenotypic characteristics. The ABM module recapitulates the heterogeneity and spatio-temporal phenomena in a tumor. In our current spQSP platform, cancer cells have three distinctive states (stem-like, progenitor, and senescent) and express distinctive neoantigens based on available scRNA-seq data. In addition, CD8+ T-cells can be further categorized by their TCR. Therefore, the ABM module captures more realistic immune/tumor interaction by recapitulating T-cell specificity and enables direct integration of single cells from high-throughput data to initialize the model. Leveraging the available public domain data, we focused this study on the integration of single cell data from tumor cells. Simulations based on this patient-specific distribution of tumor cells confirm that high antigen expression as well as homogeneity in antigen expression are associated with immunotherapy response. Although the initial condition of the ABM module relied on non-spatially resolved scRNA-seq data, we can still compare our simulated data with available multiplexed spatial data qualitatively. Our results demonstrate the spQSP model reflects the spatial distribution of tumor microenvironments that are sensitive and resistant to immunotherapy, providing a foundation to

demonstrate that this model is a suitable platform for incorporating omics data with high spatio-temporal resolution.

The integration of a comprehensive spatial computational model and highly personalized data will facilitate designing optimal treatment regimens. However, we recognize that the current spQSP model has limitations. First, we observed that cancer cells grow slower between days 15 and 30, which might not reflect the real biological processes. This indicates the QSP and ABM modules might require tighter coupling in subsequent versions of the model. The need for a stricter coupling between two modules is also reflected in the sensitivity analysis. The maximum Treg number in the tumor has a smaller impact on Treg abundance in the ABM module compared to QSP module (Figure 14). The tumor Treg recruitment in the QSP module is capped by the maximum Treg density in the tumor and the tumor volume. However, we removed the maximum capacity of Treg cells since the tumor volume is not clearly defined in the ABM module (as we only consider one or several region of interest (ROI) volumes and scale the results to the whole tumor). Secondly, some critical cell types, such as fibroblasts and macrophages are currently not explicitly accounted for in the model. Even though the immunosuppressive effect of macrophages is included implicitly in the QSP module, those cells need to be introduced explicitly in the future to represent a more comprehensive tumor immune landscape. Mi et al. have shown that the invasive front (IF) of TNBC tumors plays a significant role in forming tumor immune landscape, and the immune architecture is spatially heterogeneous especially between the IF and core regions of the tumor (Mi et al., 2020). Including normal tissue into our current spQSP platform will help tracking the dynamics of tumor IF and better defining tumor volume in the ABM module. Due to the COVID-19 pandemics, many clinical results were delayed. Therefore, we used public data as the sources of high throughput data without the

follow-up result. In the next project, the tumor progression prediction will be compared with the post-treatment outcome, which serves as the most convincing data to test the predicting power of our model.

The modeling of cellular agents of the tumor in the spQSP model provides the framework by which to integration scRNA-seq profiles into our spQSP model. As mentioned previously, these simulations have demonstrated the feasibility of leveraging high-throughput data to simulate a patient-specific tumor microenvironment. Here, we have incorporated tumor neoantigen expression from scRNA-seq into the spQSP model, and built extensive computational model using omics data. While this current study focused on tumor cells, future studies with comprehensive single cell characterization of both tumor and immune cells can be used to also initialize the immune cell composition in the computational model directly, expanding to the spatial organization for emerging spatial molecular platforms. Beyond cell types, single cell RNA-seq also captures additional biological features including cellular proliferation, cell state transitions, and signaling pathways not directly modeled in the agents in the tumor compartment of our spQSP model. To integrate newly discovered pathways, appropriate computational models are required to describe cell-to-cell interactions and protein expression dynamics. The conventional computational models include, but not limited to, mechanistic models (Bouhaddou et al., 2018; Zhao et al., 2019, 2021), statistical models (Avanzini & Antal, 2019; Szczurek et al., 2020), and data-driven models (Aguilar et al., 2020).

All model structures require certain extent of prior knowledge. Due to complexity and noise of the biological system, the prior knowledge obtained even from single cell data can be either insufficient or pretreatment data can fail to account for evolutionary processes in an individual tumor that are not modeled in our spQSP model. Those challenges lead to inaccurate

treatment outcome predictions for individual patients. A potential solution is using machine learning to train the optimal parameter sets on a defined mechanistic model (Yuan et al., 2021). In conclusion, spatially-resolved computational models driven by high-throughput data should provide insights into intra- and inter-tumoral heterogeneity and interactions between immunotherapy and other therapies and the tumor microenvironment.

5. References

Aguilar, B., Gibbs, D. L., Reiss, D. J., McConnell, M., Danziger, S. A., Dervan, A., Trotter, M., Bassett, D., Hershberg, R., Ratushny, A. V., & Shmulevich, I. (2020). A generalizable data-driven multicellular model of pancreatic ductal adenocarcinoma. *GigaScience*, *9*(7), 1–15. https://doi.org/10.1093/gigascience/giaa075

Andersson, A., Larsson, L., Stenbeck, L., Salmén, F., Ehinger, A., Wu, S., Al-Eryani, G., Roden, D., Swarbrick, A., Borg, Å., Frisén, J., Engblom, C., & Lundeberg, J. (2020). Spatial deconvolution of HER2-positive breast tumors reveals novel intercellular relationships. *BioRxiv*, 1–64. https://doi.org/10.1101/2020.07.14.200600

Avanzini, S., & Antal, T. (2019). Cancer recurrence times from a branching process model. *PLoS Computational Biology*, *15*(11), 1–30. https://doi.org/10.1371/journal.pcbi.1007423

Azizi, E., Carr, A. J., Plitas, G., Cornish, A. E., Konopacki, C., Prabhakaran, S., Nainys, J., Wu, K., Kiseliovas, V., Setty, M., Choi, K., Fromme, R. M., Dao, P., McKenney, P. T., Wasti, R. C., Kadaveru, K., Mazutis, L., Rudensky, A. Y., & Pe'er, D. (2018). Single-Cell Map of Diverse Immune Phenotypes in the Breast Tumor Microenvironment. *Cell*, *174*(5), 1293-1308.e36. https://doi.org/10.1016/j.cell.2018.05.060

Bai, J. P. F., Earp, J. C., & Pillai, V. C. (2019). Translational Quantitative Systems Pharmacology in Drug Development: from Current Landscape to Good Practices. *AAPS Journal*, *21*(4), 1–13. https://doi.org/10.1208/s12248-019-0339-5

Benvenuto, M., Focaccetti, C., Izzi, V., Masuelli, L., Modesti, A., & Bei, R. (2019). Tumor antigens heterogeneity and immune response-targeting neoantigens in breast cancer. *Seminars in Cancer Biology*, *September*, 1–12. https://doi.org/10.1016/j.semcancer.2019.10.023

Bianchini, G., Balko, J. M., Mayer, I. A., Sanders, M. E., & Gianni, L. (2016). Triple-negative breast cancer: Challenges and opportunities of a heterogeneous disease. *Nature Reviews Clinical Oncology*, *13*(11), 674–690. https://doi.org/10.1038/nrclinonc.2016.66

Bouhaddou, M., Barrette, A. M., Stern, A. D., Koch, R. J., DiStefano, M. S., Riesel, E. A., Santos, L. C., Tan, A. L., Mertz, A. E., & Birtwistle, M. R. (2018). A mechanistic pan-cancer pathway model informed by multi-omics data interprets stochastic cell fate responses to drugs and mitogens. In *PLoS Computational Biology* (Vol. 14, Issue 3). https://doi.org/10.1371/journal.pcbi.1005985

Bray, F., Ferlay, J., Soerjomataram, I., Siegel, R. L., Torre, L. A., & Jemal, A. (2018). Global cancer statistics 2018: GLOBOCAN estimates of incidence and mortality worldwide for 36 cancers in 185 countries. *CA: A Cancer Journal for Clinicians*, *68*(6), 394–424. https://doi.org/10.3322/caac.21492

Brown, S. D., Warren, R. L., Gibb, E. A., Martin, S. D., Spinelli, J. J., Nelson, B. H., & Holt, R. A. (2014). Neo-antigens predicted by tumor genome meta-analysis correlate with increased patient survival. *Genome Research*, *24*(5), 743–750. https://doi.org/10.1101/gr.165985.113

Calis, J. J. A., Maybeno, M., Greenbaum, J. A., Weiskopf, D., De Silva, A. D., Sette, A., Keşmir, C., & Peters, B. (2013). Properties of MHC Class I Presented Peptides That Enhance Immunogenicity. *PLoS Computational Biology*, *9*(10). https://doi.org/10.1371/journal.pcbi.1003266

Chung, W., Eum, H. H., Lee, H. O., Lee, K. M., Lee, H. B., Kim, K. T., Ryu, H. S., Kim, S., Lee, J. E., Park, Y. H., Kan, Z., Han, W., & Park, W. Y. (2017). Single-cell RNA-seq enables comprehensive tumour and immune cell profiling in primary breast cancer. *Nature Communications*, *8*(May), 1–12. https://doi.org/10.1038/ncomms15081

Cohen, S. D., & Hindmarsh, A. C. (1996). CVODE, a stiff/nonstiff ODE solver in C. *Computers in Physics*. https://doi.org/10.1063/1.4822377

Das, D. (2011). A Survey on Cellular Automata and Its Applications. In *Communications in Computer and Information Science* (Vol. 269). https://doi.org/10.1007/978-3-642-29219-4_84

Dutta, P., Sarkissyan, M., Paico, K., Wu, Y., & Vadgama, J. V. (2018). MCP-1 is overexpressed in triple-negative breast cancers and drives cancer invasiveness and metastasis. *Breast Cancer Research and Treatment*, *170*(3), 477–486. https://doi.org/10.1007/s10549-018-4760-8

Emens, L. A. (2021). Immunotherapy in Triple-Negative Breast Cancer. *The Cancer Journal*, *27*(1). https://journals.lww.com/journalppo/Fulltext/2021/01000/Immunotherapy_in_Triple_Negative_Breast_Cancer.9.aspx

Fancello, L., Gandini, S., Pelicci, P. G., & Mazzarella, L. (2019). Tumor mutational burden quantification from targeted gene panels: Major advancements and challenges. *Journal for ImmunoTherapy of Cancer*, *7*(1), 1–13. https://doi.org/10.1186/s40425-019-0647-4

Francis, K., & Palsson, B. O. (1997). Effective intercellular communication distances are determined by the relative time constants for cyto/chemokine secretion and diffusion. *Proceedings of the National Academy of Sciences of the United States of America*, *94*(23), 12258–12262. https://doi.org/10.1073/pnas.94.23.12258

Fumet, J. D., Truntzer, C., Yarchoan, M., & Ghiringhelli, F. (2020). Tumour mutational burden as a biomarker for immunotherapy: Current data and emerging concepts. *European Journal of Cancer*, *131*, 40–50. https://doi.org/10.1016/j.ejca.2020.02.038

Gejman, R. S., Chang, A. Y., Jones, H. F., Dikun, K., Hakimi, A. A., Schietinger, A., & Scheinberg, D. A. (2018). Rejection of immunogenic tumor clones is limited by clonal fraction. *ELife*, *7*, 1–22. https://doi.org/10.7554/eLife.41090

Ghaffarizadeh, A., Friedman, S. H., & MacKlin, P. (2016). BioFVM: An efficient, parallelized diffusive transport solver for 3-D biological simulations. *Bioinformatics*, *32*(8), 1256–1258. https://doi.org/10.1093/bioinformatics/btv730

Glanville, J., Huang, H., Nau, A., Hatton, O., Wagar, L. E., Rubelt, F., Ji, X., Han, A., Krams, S. M., Pettus, C., Haas, N., Arlehamn, C. S. L., Sette, A., Boyd, S. D., Scriba, T. J., Martinez, O. M., & Davis, M. M. (2017). Identifying specificity groups in the T cell receptor repertoire. *Nature*, *547*(7661), 94–98. https://doi.org/10.1038/nature22976

Gong, C., Milberg, O., Wang, B., Vicini, P., Narwal, R., Roskos, L., & Popel, A. S. (2017). A computational multiscale agent-based model for simulating spatio-temporal tumour immune response to PD1 and PDL1 inhibition. *Journal of the Royal Society Interface*, *14*(134). https://doi.org/10.1098/rsif.2017.0320

Goodman, A. M., Kato, S., Bazhenova, L., Patel, S. P., Frampton, G. M., Miller, V., Stephens, P. J., Daniels, G. A., & Kurzrock, R. (2017). Tumor mutational burden as an independent predictor of response to immunotherapy in diverse cancers. *Molecular Cancer Therapeutics*, *16*(11), 2598–2608. https://doi.org/10.1158/1535-7163.MCT-17-0386

Gourraud, P. A., Khankhanian, P., Cereb, N., Yang, S. Y., Feolo, M., Maiers, M., Rioux, J. D., Hauser, S., & Oksenberg, J. (2014). HLA diversity in the 1000 genomes dataset. *PLoS ONE*, *9*(7). https://doi.org/10.1371/journal.pone.0097282

Groth, C., Hu, X., Weber, R., Fleming, V., Altevogt, P., Utikal, J., & Umansky, V. (2019). Immunosuppression mediated by myeloid-derived suppressor cells (MDSCs) during tumour progression. *British Journal of Cancer*, *120*(1), 16–25. https://doi.org/10.1038/s41416-018-0333-1

Guo, X., Zhang, Y., Zheng, L., Zheng, C., Song, J., Zhang, Q., Kang, B., Liu, Z., Jin, L., Xing, R., Gao, R., Zhang, L., Dong, M., Hu, X., Ren, X., Kirchhoff, D., Roider, H. G., Yan, T., & Zhang, Z. (2018). Global characterization of T cells in non-small-cell lung cancer by single-cell sequencing. *Nature Medicine*, *24*(7), 978–985. https://doi.org/10.1038/s41591-018-0045-3

Hakim, T. S., Sugimori, K., Camporesi, E. M., & Anderson, G. (1996). Half-life of nitric oxide in aqueous solutions with and without haemoglobin. *Physiological Measurement*, *17*(4), 267–277. https://doi.org/10.1088/0967-3334/17/4/004

Han, J., Duan, J., Bai, H., Wang, Y., Wan, R., Wang, X., Chen, S., Tian, Y., Wang, D., Fei, K., Yao, Z., Wang, S., Lu, Z., Wang, Z., & Wang, J. (2020). TCR repertoire diversity of peripheral PD-1þCD8þ T cells predicts clinical outcomes after immunotherapy in patients with non–small cell lung cancer. *Cancer Immunology Research*, *8*(1), 146–154. https://doi.org/10.1158/2326-6066.CIR-19-0398

He, B., Bergenstråhle, L., Stenbeck, L., Abid, A., Andersson, A., Borg, Å., Maaskola, J., Lundeberg, J., & Zou, J. (2020). Integrating spatial gene expression and breast tumour morphology via deep learning. *Nature Biomedical Engineering*, *4*(8), 827–834. https://doi.org/10.1038/s41551-020-0578-x

Helmlinger, G., Sokolov, V., Peskov, K., Hallow, K. M., Kosinsky, Y., Voronova, V., Chu, L., Yakovleva, T., Azarov, I., Kaschek, D., Dolgun, A., Schmidt, H., Boulton, D. W., & Penland, R. C. (2019). Quantitative Systems Pharmacology: An Exemplar Model-Building Workflow With Applications in Cardiovascular, Metabolic, and Oncology Drug Development. *CPT: Pharmacometrics and Systems Pharmacology*, *8*(6), 380–395. https://doi.org/10.1002/psp4.12426

Helton, J. C., & Davis, F. J. (2003). Latin hypercube sampling and the propagation of uncertainty in analyses of complex systems. *Reliability Engineering and System Safety*, *81*(1), 23–69. https://doi.org/10.1016/S0951-8320(03)00058-9

Huang, B., Lei, Z., Zhao, J., Gong, W., Liu, J., Chen, Z., Liu, Y., Li, D., Yuan, Y., Zhang, G. M., & Feng, Z. H. (2007). CCL2/CCR2 pathway mediates recruitment of myeloid suppressor cells to cancers. *Cancer Letters*, *252*(1), 86–92. https://doi.org/10.1016/j.canlet.2006.12.012

Huang, M., Wang, J., Torre, E., Dueck, H., Shaffer, S., Bonasio, R., Murray, J. I., Raj, A., Li, M., & Zhang, N. R. (2018). SAVER: Gene expression recovery for single-cell RNA sequencing. *Nature Methods*, *15*(7), 539–542. https://doi.org/10.1038/s41592-018-0033-z

Jackson, H. W., Fischer, J. R., Zanotelli, V. R. T., Ali, H. R., Mechera, R., Soysal, S. D., Moch, H., Muenst, S., Varga, Z., Weber, W. P., & Bodenmiller, B. (2020). The single-cell pathology landscape of breast cancer. *Nature*, *578*(7796), 615–620. https://doi.org/10.1038/s41586-019-1876-x

Jafarnejad, M., Gong, C., Gabrielson, E., Bartelink, I. H., Vicini, P., Wang, B., Narwal, R., Roskos, L., & Popel, A. S. (2019). A Computational Model of Neoadjuvant PD-1 Inhibition in Non-Small Cell Lung Cancer. *AAPS Journal*, *21*(5). https://doi.org/10.1208/s12248-019-0350-x

Jiang, T., Shi, T., Zhang, H., Hu, J., Song, Y., Wei, J., Ren, S., & Zhou, C. (2019). Tumor neoantigens: From basic research to clinical applications. *Journal of Hematology and Oncology*, *12*(1), 1–13. https://doi.org/10.1186/s13045-019-0787-5

Johnson, K., Howard, G. R., Morgan, D., Brenner, E. A., Gardner, A. L., Durrett, R. E., Mo, W., Al'Khafaji, A., Sontag, E. D., Jarrett, A. M., Yankeelov, T. E., & Brock, A. (2020). Integrating multimodal data sets into a mathematical framework to describe and predict therapeutic resistance in cancer. *BioRxiv*, 2020.02.11.943738. https://doi.org/10.1101/2020.02.11.943738

Jurtz, V., Paul, S., Andreatta, M., Marcatili, P., Peters, B., & Nielsen, M. (2017). NetMHCpan-4.0: Improved Peptide–MHC Class I Interaction Predictions Integrating Eluted Ligand and Peptide Binding Affinity Data. *The Journal of Immunology*, *199*(9), 3360–3368. https://doi.org/10.4049/jimmunol.1700893

Kazdal, D., Endris, V., Allgäuer, M., Kriegsmann, M., Leichsenring, J., Volckmar, A. L., Harms, A., Kirchner, M., Kriegsmann, K., Neumann, O., Brandt, R., Talla, S. B., Rempel, E., Ploeger, C., von Winterfeld, M., Christopoulos, P., Merino, D. M., Stewart, M., Allen, J., … Stenzinger, A. (2019). Spatial and Temporal Heterogeneity of Panel-Based Tumor Mutational Burden in Pulmonary Adenocarcinoma: Separating Biology From Technical Artifacts. *Journal of Thoracic Oncology*, *14*(11), 1935–1947. https://doi.org/10.1016/j.jtho.2019.07.006

Keren, L., Bosse, M., Marquez, D., Angoshtari, R., Jain, S., Varma, S., Yang, S. R., Kurian, A., Van Valen, D., West, R., Bendall, S. C., & Angelo, M. (2018). A Structured Tumor-Immune Microenvironment in Triple Negative Breast Cancer Revealed by Multiplexed Ion Beam Imaging. *Cell*, *174*(6), 1373-1387.e19. https://doi.org/10.1016/j.cell.2018.08.039

Lazarou, G., Chelliah, V., Small, B. G., Walker, M., Graaf, P. H., & Kierzek, A. M. (2020). Integration of Omics Data Sources to Inform Mechanistic Modeling of Immune-Oncology Therapies: A Tutorial for Clinical Pharmacologists. *Clinical Pharmacology & Therapeutics*, *0*(0), 1–13. https://doi.org/10.1002/cpt.1786

Lim, B., Lin, Y., & Navin, N. (2020). Advancing Cancer Research and Medicine with Single-Cell Genomics. *Cancer Cell*, *37*(4), 456–470. https://doi.org/10.1016/j.ccell.2020.03.008

Liu, F., Lang, R., Zhao, J., Zhang, X., Pringle, G. A., Fan, Y., Yin, D., Gu, F., Yao, Z., & Fu, L. (2011). CD8+ cytotoxic T cell and FOXP3+ regulatory T cell infiltration in relation to breast cancer survival and molecular subtypes. *Breast Cancer Research and Treatment*, *130*(2), 645–655. https://doi.org/10.1007/s10549-011-1647-3

Ma, H., Wang, H., Sové, R. J., Wang, J., Giragossian, C., & Popel, A. S. (2020). Combination therapy with T cell engager and PD-L1 blockade enhances the antitumor potency of T cells as predicted by a QSP model. *Journal for ImmunoTherapy of Cancer*, *8*(2), 1–11. https://doi.org/10.1136/jitc-2020-001141

Ma, L., Hernandez, M. O., Zhao, Y., Mehta, M., Tran, B., Kelly, M., Rae, Z., Hernandez, J. M., Davis, J. L., Martin, S. P., Kleiner, D. E., Hewitt, S. M., Ylaya, K., Wood, B. J., Greten, T. F., & Wang, X. W. (2019). Tumor Cell Biodiversity Drives Microenvironmental Reprogramming in Liver Cancer. *Cancer Cell*, *36*(4), 418-430.e6. https://doi.org/10.1016/j.ccell.2019.08.007

Ma, Y., Zhu, C., Ma, P., & Yu, K. T. (2005). Studies on the diffusion coefficients of amino acids in aqueous solutions. *Journal of Chemical and Engineering Data*, *50*(4), 1192–1196. https://doi.org/10.1021/je049582g

Maleki Vareki, S. (2018). High and low mutational burden tumors versus immunologically hot and cold tumors and response to immune checkpoint inhibitors. *Journal for ImmunoTherapy of Cancer*, *6*(1), 4–8. https://doi.org/10.1186/s40425-018-0479-7

Malhotra, M. K., & Emens, L. A. (2020). The evolving management of metastatic triple negative breast cancer. *Seminars in Oncology*, *47*(4), 229–237. https://doi.org/10.1053/j.seminoncol.2020.05.005

Marino, S., Hogue, I. B., Ray, C. J., & Kirschner, D. E. (2008). A methodology for performing global uncertainty and sensitivity analysis in systems biology. *Journal of Theoretical Biology*, *254*(1), 178–196. https://doi.org/10.1016/j.jtbi.2008.04.011

Marusyk, A., Janiszewska, M., & Polyak, K. (2020). Intratumor Heterogeneity: The Rosetta Stone of Therapy Resistance. *Cancer Cell*, *37*(4), 471–484. https://doi.org/10.1016/j.ccell.2020.03.007

McGranahan, N., Furness, A. J. S., Rosenthal, R., Ramskov, S., Lyngaa, R., Saini, S. K., Jamal-Hanjani, M., Wilson, G. A., Birkbak, N. J., Hiley, C. T., Watkins, T. B. K., Shafi, S., Murugaesu, N., Mitter, R., Akarca, A. U., Linares, J., Marafioti, T., Henry, J. Y., Van Allen, E. M., … Swanton, C. (2016). Clonal neoantigens elicit T cell immunoreactivity and sensitivity to immune checkpoint blockade. *Science*, *351*(6280), 1463–1469. https://doi.org/10.1126/science.aaf1490

Mi, H., Gong, C., Sulam, J., Fertig, E. J., Szalay, A. S., Jaffee, E. M., Stearns, V., Emens, L. A., Cimino-Mathews, A. M., & Popel, A. S. (2020). Digital Pathology Analysis Quantifies Spatial Heterogeneity of CD3, CD4, CD8, CD20, and FoxP3 Immune Markers in Triple-Negative Breast Cancer. *Frontiers in Physiology*, *11*(October), 1–22. https://doi.org/10.3389/fphys.2020.583333

Norton, K. A., Jin, K., & Popel, A. S. (2018). Modeling triple-negative breast cancer heterogeneity: Effects of stromal macrophages, fibroblasts and tumor vasculature. *Journal of Theoretical Biology*, *452*, 56–68. https://doi.org/10.1016/j.jtbi.2018.05.003

Planes-Laine, G., Rochigneux, P., Bertucci, F., Chrétien, A. S., Viens, P., Sabatier, R., & Gonçalves, A. (2019). PD-1/PD-l1 targeting in breast cancer: The first clinical evidences are emerging. a literature review. *Cancers*, *11*(7), 1–25. https://doi.org/10.3390/cancers11071033

Rizvi, N. A., Hellmann, M. D., Snyder, A., Kvistborg, P., Makarov, V., Havel, J. J., Lee, W., Yuan, J., Wong, P., Ho, T. S., Miller, M. L., Rekhtman, N., Moreira, A. L., Ibrahim, F., Bruggeman, C., Gasmi, B., Zappasodi, R., Maeda, Y., Sander, C., … Chan, T. A. (2015). Mutational landscape determines sensitivity to PD-1 blockade in non-small cell lung cancer. *Science*, *348*(6230), 124–128. https://doi.org/10.1126/science.aaa1348

Rooney, M. S., Shukla, S. A., Wu, C. J., Getz, G., & Hacohen, N. (2015). Molecular and genetic properties of tumors associated with local immune cytolytic activity. *Cell*, *160*(1–2), 48–61. https://doi.org/10.1016/j.cell.2014.12.033

Rozenblatt-Rosen, O., Regev, A., Oberdoerffer, P., Nawy, T., Hupalowska, A., Rood, J. E., Ashenberg, O., Cerami, E., Coffey, R. J., Demir, E., Ding, L., Esplin, E. D., Ford, J. M., Goecks, J., Ghosh, S., Gray, J. W., Guinney, J., Hanlon, S. E., Hughes, S. K., … Zhuang, X. (2020). The Human Tumor Atlas Network: Charting Tumor Transitions across Space and Time at Single-Cell Resolution. *Cell*, *181*(2), 236–249. https://doi.org/10.1016/j.cell.2020.03.053

Schimke, R. T. (1964). The Importance of Both Synthesis and Degradation in the Control of Arginase Levels in Rat Liver. *Journal of Biological Chemistry*, *239*(11), 3808–3817. https://doi.org/10.1016/s0021-9258(18)91209-3

Schweighofer, N., & Ferriol, G. (2000). Diffusion of nitric oxide can facilitate cerebellar learning: A simulation study. *Proceedings of the National Academy of Sciences of the United States of America*, *97*(19), 10661–10665. https://doi.org/10.1073/pnas.97.19.10661

Serafini, P., Mgebroff, S., Noonan, K., & Borrello, I. (2008). Myeloid-derived suppressor cells promote cross-tolerance in B-cell lymphoma by expanding regulatory T cells. *Cancer Research*, *68*(13), 5439–5449. https://doi.org/10.1158/0008-5472.CAN-07-6621

Singh, N. K., Riley, T. P., Baker, S. C. B., Borrman, T., Weng, Z., & Baker, B. M. (2017). Emerging Concepts in TCR Specificity: Rationalizing and (Maybe) Predicting Outcomes. *The Journal of Immunology*, *199*(7), 2203–2213. https://doi.org/10.4049/jimmunol.1700744

Sové, R. J., Jafarnejad, M., Zhao, C., Wang, H., Ma, H., & Popel, A. S. (2020). QSP-IO: A Quantitative Systems Pharmacology Toolbox for Mechanistic Multiscale Modeling for Immuno-Oncology Applications. *CPT: Pharmacometrics and Systems Pharmacology*, *9*(9), 484–497. https://doi.org/10.1002/psp4.12546

Stamatelos, S. K., Bhargava, A., Kim, E., Popel, A. S., & Pathak, A. P. (2019). Tumor Ensemble-Based Modeling and Visualization of Emergent Angiogenic Heterogeneity in Breast Cancer. *Scientific Reports*, *9*(1), 1–14. https://doi.org/10.1038/s41598-019-40888-w

Stamatelos, S. K., Kim, E., Pathak, A. P., & Popel, A. S. (2014). A bioimage informatics based reconstruction of breast tumor microvasculature with computational blood flow predictions. *Microvascular Research*, *91*, 8–21. https://doi.org/10.1016/j.mvr.2013.12.003

Szczurek, E., Krüger, T., Klink, B., & Beerenwinkel, N. (2020). A mathematical model of the metastatic bottleneck predicts patient outcome and response to cancer treatment. *PLoS Computational Biology*, *16*(10), 1–20. https://doi.org/10.1371/journal.pcbi.1008056

Tanimoto, A., Murata, Y., Wang, K.-Y., Tsutsui, M., Kohno, K., & Sasaguri, Y. (2008). Monocyte chemoattractant protein-1 expression is enhanced by granulocyte-macrophage colony-stimulating factor via Jak2-Stat5 signaling and inhibited by atorvastatin in human monocytic U937 cells. *The Journal of Biological Chemistry*, *283*(8), 4643–4651. https://doi.org/10.1074/jbc.M708853200

Topalian, S. L., Taube, J. M., & Pardoll, D. M. (2020). Neoadjuvant checkpoint blockade for cancer immunotherapy. *Science*, *367*(6477). https://doi.org/10.1126/science.aax0182

Vroman, H., Balzaretti, G., Belderbos, R. A., Klarenbeek, P. L., Van Nimwegen, M., Bezemer, K., Cornelissen, R., Niewold, I. T. G., Van Schaik, B. D., Van Kampen, A. H., Aerts, J. G. J. V., De Vries, N., & Hendriks, R. W. (2020). T cell receptor repertoire characteristics both before and following immunotherapy correlate with clinical response in mesothelioma. *Journal for ImmunoTherapy of Cancer*, *8*(1), 1–8. https://doi.org/10.1136/jitc-2019-000251

Wang, H., Ma, H., Sové, R. J., Emens, L. A., & Popel, A. S. (2021). Quantitative systems pharmacology model predictions for efficacy of atezolizumab and nab-paclitaxel in triple-negative breast cancer. *Journal for ImmunoTherapy of Cancer*, *9*(2), e002100. https://doi.org/10.1136/jitc-2020-002100

Wang, H., Sové, R. J., Jafarnejad, M., Rahmeh, S., Jaffee, E. M., Stearns, V., Torres, E. T. R., Connolly, R. M., & Popel, A. S. (2020). Conducting a Virtual Clinical Trial in HER2-Negative Breast Cancer Using a Quantitative Systems Pharmacology Model With an Epigenetic Modulator and Immune Checkpoint Inhibitors. *Frontiers in Bioengineering and Biotechnology*, *8*(February), 1–16. https://doi.org/10.3389/fbioe.2020.00141

Wu, J., Zhao, W., Zhou, B., Su, Z., Gu, X., Zhou, Z., & Chen, S. (2018). TSNAdb: A Database for Tumor-specific Neoantigens from Immunogenomics Data Analysis. *Genomics, Proteomics and Bioinformatics*, *16*(4), 276–282. https://doi.org/10.1016/j.gpb.2018.06.003

Yeong, J., Thike, A. A., Lim, J. C. T., Lee, B., Li, H., Wong, S. C., Hue, S. S. S., Tan, P. H., & Iqbal, J. (2017). Higher densities of Foxp3+ regulatory T cells are associated with better prognosis in triple-negative breast cancer. *Breast Cancer Research and Treatment*, *163*(1), 21–35. https://doi.org/10.1007/s10549-017-4161-4

Yuan, B., Shen, C., Luna, A., Korkut, A., Marks, D. S., Ingraham, J., & Sander, C. (2021). Article CellBox : Interpretable Machine Learning for Perturbation Biology with Application to the Design of Cancer Combination Therapy CellBox : Interpretable Machine Learning for Perturbation Biology with Application to the Design of Cancer Combination T. *Cell Systems*, 1–13. https://doi.org/10.1016/j.cels.2020.11.013

Zhang, J., Cai, J., Bello, A., Roy, A., & Sheng, J. (2019). Model-Based Population Pharmacokinetic Analysis of Nivolumab in Chinese Patients With Previously Treated Advanced Solid Tumors, Including Non–Small Cell Lung Cancer. *Journal of Clinical Pharmacology*, *59*(10), 1415–1424. https://doi.org/10.1002/jcph.1432

Zhao, C., Medeiros, T. X., Sové, R. J., Annex, B. H., & Popel, A. S. (2021). A data-driven computational model enables integrative and mechanistic characterization of dynamic macrophage polarization. *IScience*, 102112. https://doi.org/10.1016/j.isci.2021.102112

Zhao, C., Mirando, A. C., Sové, R. J., Medeiros, T. X., Annex, B. H., & Popel, A. S. (2019). A mechanistic integrative computational model of macrophage polarization: Implications in human pathophysiology. *PLoS Computational Biology*, *15*(11), 1–28. https://doi.org/10.1371/journal.pcbi.1007468

Zheng, C., Zheng, L., Yoo, J. K., Guo, H., Zhang, Y., Guo, X., Kang, B., Hu, R., Huang, J. Y., Zhang, Q., Liu, Z., Dong, M., Hu, X., Ouyang, W., Peng, J., & Zhang, Z. (2017). Landscape of Infiltrating T Cells in Liver Cancer Revealed by Single-Cell Sequencing. *Cell*, *169*(7), 1342-1356.e16. https://doi.org/10.1016/j.cell.2017.05.035